Computer Aided Diagnosis system for prostatic biopsy guidance and follow-up fusing multi-modal imaging.

Guillaume Lemaître

LE2I - ViCOROB

Université de Bourgogne - Universitat de Girona

Supervisors:

Jordi Freixenet Bosch (ViCOROB - UdG)

Fabrice Mériaudeau (CISIR - UTP)

Robert Marí Marly (ViCOROB - UdG)

Paul Michael Walker (LE2I - UBFC)

A thesis submitted for the degree of

PhilosophiæDoctor (PhD)

April 2015

1. Reviewer: Name

2. Reviewer:

Day of the defense:

Signature from head of PhD committee:

Abstract

Put your abstract or summary here, if your university requires it.

To ...

Acknowledgements

I would like to acknowledge the thousands of individuals who have coded for the LaTeX project for free. It is due to their efforts that we can generate professionally typeset PDFs now.

Contents

List of Abbreviations

ADC apparent diffusion coefficient

AIF arterial input function

ASM active shape model

BPH benign prostatic hyperplasia

CAD computer-aided detection and diangosis

CADe computer-aided detection

CADx computer-aided diagnosis

CaP prostate cancer

CG central gland

Chap. Chapter

CSE chemical shift effect

CZ central zone

DCE dynamic contrast-enhanced

DW diffusion weighted

EES extravascular-extracellular space

Eq. equation

ERSSPC European Randomized Study of Screening for Prostate Cancer

ES Evolution Strategy

Fig. figure

FOV field of view

FSE Fast Spin-Echo

GS Gleason score

***g*-scale** generalized scale

ITK Insight Segmentation and Registration Toolkit

LBP local binary pattern

LDA linear discriminant analysis

MANTRA multi-attribute non-initializing texture reconstruction based active shape model

MAP maximum *a posteriori*

MI mutual information

MRI magnetic resonance imaging

MRSI magnetic resonance spectroscopy imaging

NMR nuclear magnetic resonance

PDF probability density function

PLCO Prostate Lung Colorectal and Ovarian

PSA prostate-specific antigen

PZ peripheral zone

Sect. section

SI signal intensity

SNR signal-to-noise

STAPLE simultaneous truth and performance level estimation

SVD singular value decomposition

T_1-W T_1 Weighted

T_2-W T_2 Weighted

TE echo time

TPS thin plate spline

TR repetition time

TRUS transrectal ultrasound

TZ transitional zone

US ultrasound

List of Figures

List of Tables

Chapter 1

Introduction

1.1 Prostate anatomy

The prostate is an exocrine gland of the male reproductive system having an inverted pyramidal shape, which is located below the bladder and infront of the rectum (see Fig. 1.1. It measures approximately three centimetres in height by two and half centimetres in depth and its weight is estimated to be between seven and sixteen grams for an adult (5). The prostate size increases at two distinct stages during physical development: initially at puberty to reach its normal size, then again after sixty years of age leading to benign prostatic hyperplasia (BPH) (6).

A zonal classification of the prostate, depicted in Fig. 1.2, was suggested by McNeal (7). Subsequently, this categorization was widely accepted in the literature (cf., (6,

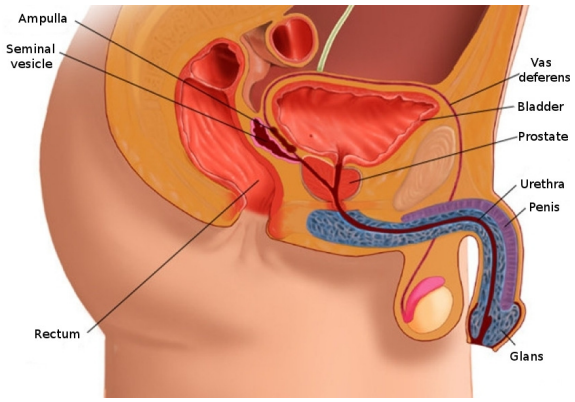

Figure 1.1: Sagittal anatomy scheme of the male reproductive system.

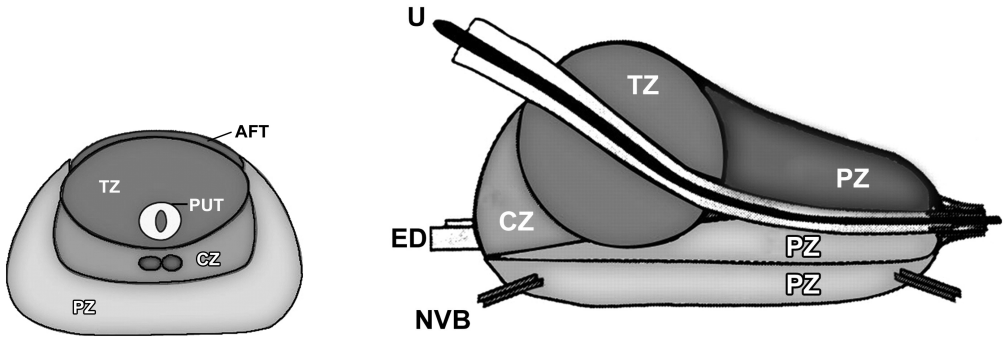

(a) Transverse anatomy of the prostate.

(b) Sagittal anatomy of the prostate.

Figure 1.2: Prostate anatomy with division in different zones. *AFT:* anterior fibromuscular tissue, *CZ:* central zone, *ED:* ejaculatory duct, *NVB:* neurovascular bundle, *PUT:* tissue, *PZ:* peripheral zone, *U:* urethra, *TZ:* transitional zone, *B:* base, *M:* median, *A:* apex (copyright by (4)).

8, 9, 10)) and is used in all medical examinations (e.g., biopsy, MRI screening. The classification is based on dividing the gland into three distinct regions: (i) central zone (CZ) accounting for 20-25% of the whole prostate gland, (ii) transitional zone (TZ) standing for 5% and (iii) peripheral zone (PZ) representing the 70%. In MRI images, tissues of CZ and TZ are difficult to distinguish and are usually merged into a common region, denominated central gland (CG). As part of this classification, the prostate can be divided in three longitudinal portions depicted in Fig. 1.2(b): (i) base, (ii) median gland and (iii) apex.

1.2 Prostate carcinoma

Prostate cancer (CaP) has been reported on a worldwide scale to be the second most frequently diagnosed cancer of men accounting for 13.6% (11). Statistically, in 2008, the number of new diagnosed cases was estimated to be $899,000$ with no less than $258,100$ deaths (11). In United States, aside from skin cancer, CaP was declared to be the most commonly diagnosed cancer among men, implying that approximately one in six men will be diagnosed with CaP during their lifetime and one in thirty-six will die from this disease causing CaP to be the second most common cause of cancer death among men

(12), (13).

Despite active research to determine the causes of prostate cancer, a fuzzy list of risk factors has arisen (14). The etiology was linked to the following factors (14): (i) family history (15, 16), (ii) genetic factors (17, 18, 19), (iii) race-ethnicity (15, 20), (iv) diet (15, 21, 22), and (v) obesity (15, 23). This list of risk factors alone cannot be used to diagnose CaP and in this way, screening enables early detection and treatment.

CaP growth is characterized by two main types of evolution (24): slow-growing tumours, accounting for up to 85 % of all CaPs (25), progress slowly and usually stay confined to the prostate gland. For such cases, treatment can be substituted with active surveillance. In contrast, the second variant of CaPs develops rapidly and metastasises from prostate gland to others organs, primarily the bones (26). Bone metastases, being an incurable disease, significantly affects the morbidity and mortality rate (27). Hence, the results of the surveillance have to be trustworthy in order to distinguish aggressive from slow-growing CaP.

CaP is more likely to come into being in specific regions of the prostate. In that respect, around 70-80 % of CaPs originate in PZ whereas 10-20 % in TZ (28, 29, 30). Only about 5 % of CaPs occur in CZ (29, 31). However, those cancers appear to be more aggressive and more likely to invade other organs due to their location (31).

1.3 CaP screening and imaging techniques

Current CaP screening consists of three different stages. First, prostate-specific antigen (PSA) control is performed to distinguish between low and high risk CaP. Then, for confirmation, samples are taken during prostate biopsy and finally analysed to evaluate the prognosis and the stage of CaP. In this section, we present a detailed description of the current screening as well as its drawbacks.

Since its introduction in mid-1980s, PSA is widely used for CaP screening (32). A higher-than-normal level of PSA can indicate an abnormality of the prostate either as a BPH or a cancer (33). However, other factors can lead to an increased PSA level such as prostate infections, irritations, a recent ejaculation or a recent rectal examination (6). PSA can be found in the bloodstream in two different forms: free PSA (about 10%), and linked to another protein (about 90%). A level of PSA higher than 10 $ng.mL^{-1}$ is considered to be at risk (6). If the PSA level is between 10 $ng.mL^{-1}$ and 4 $ng.mL^{-1}$,

the patient is considered as suspicious (34). In that case, the ratio of free PSA to total PSA is computed; if the ratio is higher than 15%, the case is considered as pathological (6).

A transrectal ultrasound (TRUS) biopsy is carried out for cases which are considered as pathological. At least six different samples are taken randomly from the right and left parts of three different zones: apex, median and base. These samples are further evaluated using the Gleason grading system (35). The scoring scheme to characterize the biopsy sample is composed of five different patterns which correspond to grades ranging from 1 to 5. Higher grades are associated with poor prognosis (36). Then, in the Gleason system, two scores are assigned corresponding to (i) the grade of the most present tumour pattern, and (ii) the grade of the second most present tumour pattern (36). A higher GS indicates a more aggressive tumour (36). Also, it should be noted that biopsy is an invasive procedure which can result in serious infection or urine retention (37, 38).

Although PSA screening has been shown to improve early detection of CaP (38), its lack of reliability motivates further investigations using MRI-CAD. Two reliable studies, carried out in the United States (39) and in Europe (40, 41), have attempted to assess the impact of early detection of CaP, with diverging outcomes (38, 42). The study carried out in Europe[1] concluded that PSA screening reduces CaP-related mortality by 21-44% (40, 41), while the American[2] trial found no such effect (39). However, both studies agree that PSA screening suffers from low specificity, with an estimated rate of 36 % (43). Both studies also agree that over-treatment is an issue: decision making regarding treatment is further complicated by difficulties in evaluating the aggressiveness and progression of CaP (44).

Hence, new screening methods should be developed with improved specificity of detection as well as more accurate risk assessment (aggressiveness and progression). Current research is focused on identifying new biological markers to replace PSA-based screening (45, 46, 47). Until such research comes to fruition, these needs can be met through active-surveillance strategy using multi-parametric MRI techniques (33, 48).

[1]The European Randomized Study of Screening for Prostate Cancer (ERSSPC) started in the 1990s in order to evaluate the effect of PSA screening on mortality rate.

[2]The Prostate Lung Colorectal and Ovarian (PLCO) cancer screening trial is carried out in the United States and intends to ascertain the effects of screening on mortality rate.

An MRI-CAD system, which is an area of active research and forms the focus of this thesis, can be incorporated into this screening strategy allowing a more systematic and rigorous follow-up.

Another weakness of the current screening strategy lies in the fact that TRUS biopsy does not provide trustworthy results. Due to its "blind" nature, there is a chance of missing aggressive tumours or detecting microfocal "cancers", which influences the aggressiveness-assessment procedure (49). As a consequence, over-diagnosis is estimated at up to 30 % (50), while missing clinically significant CaP is estimated at up to 35 % (51). In an effort to solve both issues, alternative biopsy approaches have been explored. MRI/ultrasound (US)-guided biopsy has been shown to outperform standard TRUS biopsy (52). There, multimodal MRI images are fused with US images in order to improve localization and aggressiveness assessment to carry out biopsies. Human interaction plays a major role in biopsy sampling which can lead to low repeatability; by reducing potential human errors at this stage, the CAD framework can be used to improve repeatability of examination. CaP detection and diagnosis benefit from the use of CAD and MRI techniques.

In an effort to improve the current statge of CaP diagnosis and detection, this thesis is intended to provide a multiparameteric MRI CAD system. MRI principles and its different modalites are presented in Chapter (Chap.) 2.

1.4 Computer-aided systems for CaP

During the last century, physicists have focused on constantly innovating in terms of imaging techniques assisting radiologists to improve cancer detetction and diagnosis. However, human diagnosis still suffers from low repeatability, synonymous with erroneous detection or interpretations of abnormalities throughout clinical decisions (53, 54). These errors are driven by two majors causes (53): observer limitations (e.g., constrained human visual perception, fatigue or distraction) and the complexity of the clinical cases themselves, for instance due to unbalanced data (number of healthy cases more abundant than malignant cases) or overlapping structures.

Computer vision has given rise to many promising solutions, but, instead of focusing on fully automatic computerized systems, researchers have aimed at providing computer image analysis techniques to aid radiologists in their clinical decisions (53). In fact,

these investigations brought about both concepts of computer-aided detection (CADe) and computer-aided diagnosis (CADx) grouped under the acronym CAD. Since those first steps, evidence has shown that CAD systems enhance the diagnosis performance of radiologists. Chan *et al.* reported a significant 4 % improvement in breast cancer detection (55), which has been confirmed in later studies (56). Similar conclusions were drawn in the case of lung nodule detection (57), colon cancer (58) and CaP as well (54). Chan *et al.* (55) also hypothesized that CAD systems will be even more efficient assisting inexperienced radiologists than senior radiologists. That hypothesis was tested by Hambrock *et al.* (54) and was confirmed in case of CaP detection. In this particular study, inexperienced radiologists obtained equivalent performance to senior radiologists, both using CAD whereas the accuracy of their diagnosis was significantly poorer without CAD's help.

In contradiction with the aforementioned statement, CAD for CaP is a young technology due to the fact that is based on MRI (59). Four distinct MRI modalities are employed in CaP diagnosis which were mainly developed after the mid-1990s: (i) T_2-W MRI (60), (ii) DCE MRI (61), (iii) MRSI (62) and (iv) DW MRI (63). In addition, the increase of magnetic field strength (from 1.5 to 3 Tesla) and the development of endorectal coils, both imporved image spatial resolution (64) needed to perform more accurate diagnosis. It is for this matter that the development of CAD for CaP is still lagging behind fields stated above.

This research is aimed at first, to provide an overview of the current state-of-the-art of CAD for CaP and later, according to the drawn coclusions, to propose a CAD which takes advantag of multiparameteric MRI modalities. A review of the current proposed CAD for CaP is presented in Chap. 3.

1.5 Research motivation

1.6 Thesis outline

Chapter 2

MRI Principles and Imaging Techniques

2.1 MRI principles

2.2 MRI imaging techniques

MRI provides promising imaging techniques to overcome the previous mentioned drawbacks. Unlike TRUS biopsy, MRI examination is a non-invasive protocol and has been shown to be the most acute and harmless technique available currently (65). In this section, we review different MRI techniques developed for CaP detection and diagnosis. Features strengthening each modality, will receive particular attention together with their drawbacks. Commonly, these features form the basis for developing analytic tools and automatic algorithms. However, we refer the reader to Sect.. **??** for more details on automatic feature detection methods since they are part and parcel of the CAD framework. Table 2.1 provides an overview of the following discussion.

2.2.1 T_2-W MRI

T_2-W MRI was the first MRI-modality used to perform CaP diagnosis using MRI (60). Nowadays, radiologists make use of it for CaP detection, localization and staging purposes. This imaging technique is well suited to render zonal anatomy of the prostate (34).

Table 2.1: Overview of the features associated with each MRI modality. Acronyms: prostate cancer (CaP) - signal intensity (SI) - Gleason score (GS).

Modality	Significant features	CaP	Healthy tissue	GS correlation
T_2-W MRI	SI	low-SI	intermediate to high-SI	+
T_2 map	SI	low-SI	intermediate to high-SI	+
DCE MRI	Semi-quantitative features:			
	– wash-in	faster	slower	0
	– wash-out	faster	slower	0
	– integral under the curve	higher	lower	0
	– maximum signal intensity	higher	lower	0
	– time-to-peak enhancement	faster	slower	0
	Quantitative features (Tofts' parameters):			
	– k_{ep}	higher	lower	0
	– K^{trans}	higher	lower	0
DW MRI	SI	higher-SI	lower-SI	+
ADC map	SI	low-SI	high-SI	+
MRSI	Metabolites:			
	Citrate (2.64 ppm)	lower concentration	higher concentration	+
	Choline (3.21 ppm)	higher concentration	lower concentration	0
	Spermine (3.11 ppm)	lower concentration	higher concentration	+

Notes:
+ = significantly correlated.
0 = no correlation.

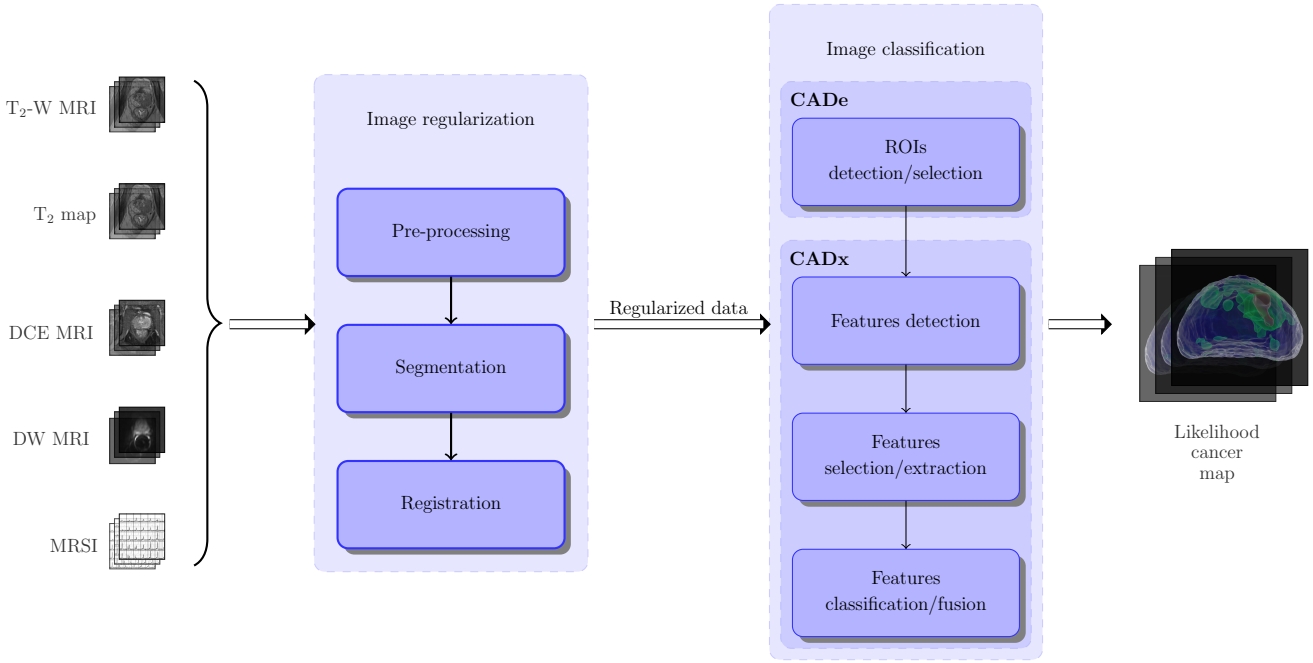

Figure 2.1: CAD framework using MRI images. Multiparametric MRI images are provided as inputs. These data arise from heterogeneous sources and need to be regularized. Some studies do not consider this stage as mandatory and do not implement or only partly those processes (see Tab. 3.1). A pre-processing stage is usually applied to standardize the intensity of images, reduce noise and artefacts. Then, in the image set, the prostate organ has to be segmented to focus the next processing stages only on that particular ROI. Moreover, prostate location can vary depending of the modality chosen. Therefore, the images are registered so that all segmented images will be in the same reference frame. Once the image regularisation performed, image classification can be carried out. First, a strategy defining ROIs to focus on is decided. Then, distinctive features are extracted before to be post-processed to select the most salient features. Finally, these salient features will feed a classifier previously trained which will provide a likelihood cancer map associated with either CaP detection or diagnosis.

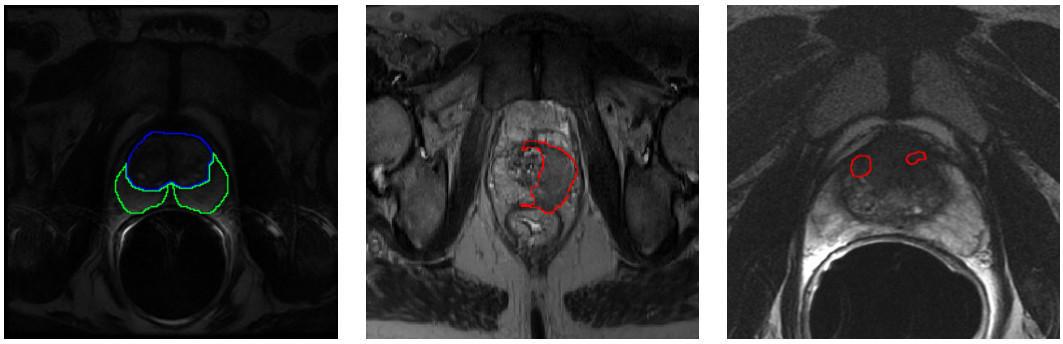

(a) T_2-W-MRI slice of an healthy prostate acquire with a 1.5 Tesla MRI. The blue contour represents the CG while the PZ corresponds to the green contour.

(b) T_2-W-MRI slice of a prostate with a CaP highlighted in the PZ using a 3.0 Tesla MRI scanner.

(c) T_2-W-MRI slice of a prostate with a CaP highlighted in the CG using a 3.0 Tesla MRI scanner.

Figure 2.2: Rendering of T_2-W-MRI prostate image with both 1.5 and 3.0 Tesla MRI scanner.

This modality relies on a sequence based on setting a long repetition time (TR), reducing the T_1 effect in nuclear magnetic resonance (NMR) signal measured, and fixing the echo time (TE) to sufficiently large values in order to enhance the T_2 effect of tissues. Thus, PZ and CG tissues are well perceptible in these images. The former is characterized by an intermediate/high-SI while the latter is depicted by a low-SI (8). An example of a healthy prostate is shown in Fig. 2.2(a).

In PZ, round or ill-defined low-SI masses are synonymous with CaPs (60) as shown in Fig. 2.2(b). Detecting CaP in CG is more challenging. In fact both normal CG tissue and malignant tissue, have a low-SI in T_2-W MRI reinforcing difficulties to distinguish between them. However, CaPs in CG appear often as homogeneous mass possessing ill-defined edges with lenticular or "water-drop" shapes (34, 66) as depicted in Fig. 2.2(c).

CaP aggressiveness was shown to be inversely correlated with SI. Indeed, CaPs assessed with a GS of 4-5 implied lower SI than the one with a GS of 2-3 (67).

In spite of the availability of these useful and encouraging features, the T_2-W modality lacks reliability (33, 68). Sensitivity is affected by the difficulties in detecting cancers in CG (68) while specificity rate is highly affected by outliers (34). In fact, various conditions emulate patterns of CaP such as BPH, post-biopsy haemorrhage, atrophy, scars

and post-treatment (8, 34, 63, 69, 70). These issues can be partly addressed using more innovative and advanced modalities.

2.2.2 T_2 map

As previously mentioned, T_2-W MRI modality shows low sensitivity. Moreover, T_2-W MRI images are a composite of multiple effects (59). However, T_2 values alone have been shown to be more discriminative (71) and highly correlated with citrate concentration, a biological marker in CaP (72, 73).

T_2 values are computed using the characteristics of transverse relaxation which is formalized as:

$$M_{x,y}(t) = M_{x,y}(0) \exp\left(-\frac{t}{\mathrm{T}_2}\right) , \tag{2.1}$$

where $M_{x,y}(0)$ is the initial value of $M_{x,y}(t)$ and T_2 is the relaxation time. By rearranging Eq. 2.1, T_2 map is computed performing a linear fitting on the model in Eq. 2.2 using several TE, $t = \{\mathrm{TE}_1, \mathrm{TE}_2, \ldots, \mathrm{TE}_m\}$.

$$\ln\left[\frac{M_{x,y}(t)}{M_{x,y}(0)}\right] = -\frac{t}{\mathrm{T}_2} . \tag{2.2}$$

The Fast Spin-Echo (FSE) sequence has been shown to be particularly well suited in order to build a T_2 map and obtain accurate T_2 values (74). Similar to T_2-W MRI, T_2 values associated with CaP are significantly lower than those of healthy tissues (72, 75).

2.2.3 DCE MRI

DCE MRI is an imaging technique which exploits the vascularity characteristic of tissues. Contrast media, usually gadolinium-based, is injected intravenously into the patient. The media extravasates from vessels to extravascular-extracellular space (EES) and is released back into the vasculature before being eliminated by the kidneys (76). Furthermore, the diffusion speed of the contrast agent may vary due to several parameters: (i) the permeability of the micro-vessels, (ii) their surface area and (iii) the blood flow (77).

Healthy PZ is mainly made up of glandular tissue, around 70 % (4), which implies a reduced interstitial space restricting exchanges between vessels and EES (78, 79). Normal CG has a more disorganised structure, composed of mainly fibrous tissue (4, 33), which

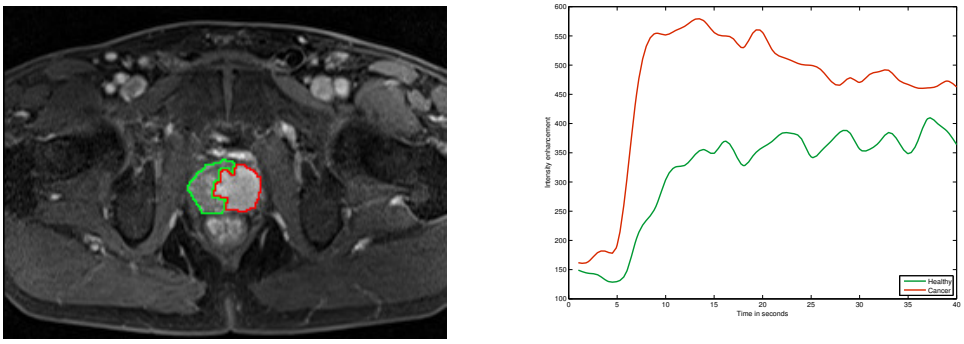

(a) T_1-W-MRI image where the cancer is delimited by the red contour. The green area was still not invaded by the CaP

(b) Enhancement curve computed during the DCE-MRI analysis. The red curve is typical from CaP cancer while the green curve is characteristic of healthy tissue.

Figure 2.3: Illustration of typical enhancement signal observed in DCE-MRI analysis collected with a 3.0 Tesla MRI scanner.

facilitates the arrival of the contrast agent in EES (80). To understand the difference between contrast media kinetic in malignant tumours and the two previous behaviours mentioned, one has to focus on the process known as angiogenesis (81). In order to ensure growth, malignant tumours produce and release angiogenic promoter substances (81). These molecules stimulate the creation of new vessels towards the tumour (81). However, the new vessel networks in tumours differ from those present in healthy tissue (76). They are more porous due to the fact that their capillary walls have a large number of "openings" (4, 76). In contrast to healthy cases, this increased vascular permeability results in increased contrast agent exchanges between vessels and EES (82).

By making use of the previous aspects, DCE MRI is based on an acquisition of a set of T_1-W MRI images over time. The Gadolinium-based contrast agent shortens T_1 relaxation time enhancing contrast in T_1-W MRI images. The aim is to post-analyse the pharmacokinetic behaviour of the contrast media concentration in prostate tissues (82). The image analysis is carried out in two dimensions: (i) in the spatial domain on a pixel-by-pixel basis and (ii) in the time domain corresponding to the consecutive images acquired with the MRI. Thus, for each spatial location, a signal linked to contrast media concentration is measured as shown in Fig. 2.3(b) (83).

By taking the previous remarks regarding medical aspects and signal theory into

account, CaPs are characterized by a signal having an earlier and faster enhancement and an earlier wash-out (cf., the rate of the contrast agent flowing out of the tissue) (see Fig. 2.3(b)) (82). Three different approaches exist to analyse these signals with the aim of tagging them as corresponding to either normal or malignant tissues. Qualitative analysis is based on assessment of the signal shape (33).

Quantitative approaches consist of inferring pharmocokinetic parameter values (83). Those parameters are part of mathematical-pharmacokinetic models which are directly based on physiological exchanges between vessels and EES. Several pharmacokinetic models were proposed such as the Kety model (84), the Tofts model (85) and mixed models (86, 87). The last family of methods mixed both approaches and are grouped together under the heading of semi-quantitative methods. They rely on shape characterization using mathematical modelling to extract a set of parameters such as wash-in gradient, wash-out, integral under the curve, maximum signal intensity, time-to-peak enhancement and start of enhancement. These parameters will be discussed in a later section (see Fig. **??**) (33, 82). It was shown that semi-quantitative and quantitative methods improve localization of CaP when compared with qualitative methods (88). Section **??** provides a full description of quantitative and semi-quantitative approaches.

DCE MRI combined with T_2-W MRI has shown to enhance sensitivity compared to T_2-W MRI alone (89, 90, 91, 92). Despite this fact, DCE MRI possesses some drawbacks. Due to its "dynamic" nature, patient motions during the image acquisition lead to spatial misregistration of the image set (82)). Furthermore, it has been suggested that malignant tumours are difficult to distinguish from prostatitis located in PZ and BPH located in CG (33, 82). These pairs of tissues tend to have similar appearances. Later studies have shown that CaPs in CG do not always manifest in homogeneous fashion. Indeed, tumours in this zone can present both hypo-vascularization and hyper-vascularization which illustrates the challenge of CaP detection in CG (80).

2.2.4 DW MRI

As previously mentioned in the introduction, DW MRI is the most recent MRI imaging technique aiming at CaP detection and diagnosis (63). This modality exploits the variations in the motion of water molecules in different tissues (93, 94).

From a physiological point of view, the following facts can be claimed. On the one hand, PZ, as previously mentioned, is mainly glandular and tubular in structure allowing

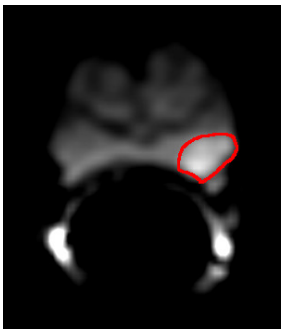

(a) DW-MRI image acquired with a 1.5 Tesla MRI scanner. The cancer corresponds to the high SI region highlighted in red.

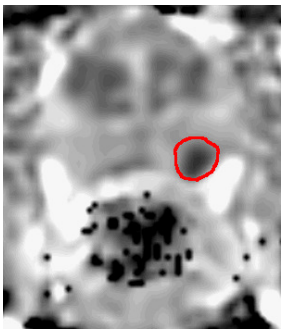

(b) ADC map computer after acquisition of DW-MRI iages with a 1.5 Tesla MRI scanner. The cancer corresponds to the low SI region highlighted in red.

Figure 2.4: Illustration of of DW-MRI and ADC map. The signal intensity corresponding to cancer are inversely correlated on these two types of imaging techniques.

water molecules to move freely (4, 33). On the other hand, CG is made up of muscular or fibrous tissue causing the motion of the water molecules to be more constrained and heterogeneous than in PZ (33). Then, CaP growth leads to the destruction of normal glandular structure and is associated with an increase in cellular density (33, 94, 95). Furthermore, these factors both have been shown to be inversely correlated with water diffusion (94, 95): higher cellular density implies a restricted water diffusion. Thus, water diffusion in CaP will be more restricted than both healthy PZ and CG (33, 94).

From the NMR principle side, DW MRI sequence produces contrasted images due to variation of water molecules motion. The method is based on the fact that the signal in DW MRI images is inversely correlated to the degree of random motion of water molecules (96). In fact, gradients are used in DW MRI modality to encode spatial location of nuclei temporarily. Simplifying the problem in only one direction, a gradient is applied in that direction, dephasing the spins of water nuclei. Hence, the spin phases vary along the gradient direction depending of the gradient intensity at those locations. Then, a second gradient is applied aiming at cancelling the spin dephasing. Thus, the immobile water molecules will be subject to the same gradient intensity as the initial one while moving water molecules will be subject to a different gradient intensity. Thus, spins

of moving water molecules will stay dephased whereas spins of immobile water molecules will come back in phase. As a consequence, a higher degree of random motion results in a more significant signal loss whereas a lower degree of random motion is synonymous with lower signal loss (96). Under these conditions, the MRI signal is measured as:

$$M_{x,y}(t,b) = M_{x,y}(0)\exp\left(-\frac{t}{\mathrm{T}_2}\right) S_{\mathrm{ADC}}(b)\ , \tag{2.3}$$

$$S_{\mathrm{ADC}}(b) = \exp\left(-b \times \mathrm{ADC}\right)\ , \tag{2.4}$$

where S_{ADC} refers to signal drop due to diffusion effect, ADC is the apparent diffusion coefficient and b is the attenuation coefficient depending only on gradient pulses parameters: (i) gradient intensity and (ii) gradient duration (97).

By using this formulation, image acquisition with a parameter $b = 0$ s.mm^{-2} corresponds to a T_2-W MRI acquisition. Then, increasing the attenuation coefficient b (cf., increase gradient intensity and duration) enhances the contrast in DW MRI images.

To summarize, in DW MRI images, CaPs are characterized by high-SI compared to normal tissues in PZ and CG as shown in Fig. 2.4(a) (34). However, some tissues in CG can look similar to CaP with higher SI (34).

Diagnosis using DW MRI combined with T_2-W MRI has shown a significant improvement compared with T_2-W MRI alone and provides highly contrasted images (4, 98, 99). As drawbacks, this modality suffers from poor spatial resolution and specificity due to false positive detection (4). With a view to eliminate these drawbacks, radiologists are extracting quantitative maps from DW MRI. This imaging technique is presented next.

2.2.5 ADC Map

The NMR signal measured for DW MRI images is not only affected by diffusion as shown in Eq. (2.3). However, the signal drop (Eq. (2.4)) is formulated such that the only variable is the acquisition parameter b (97). The ADC is considered as a "pure" diffusion coefficient and can be extracted to build a quantitative map.

From Eq. (2.3), it is clear that performing multiple acquisitions only varying b will not have any effect on the term $M_{x,y}(0)\exp\left(-\frac{t}{\mathrm{T}_2}\right)$. Thus, Eq. (2.3) can be rewritten

as:

$$S(b) = S_0 \exp\left(-b \times \text{ADC}\right) \ . \tag{2.5}$$

To compute the ADC map, a minimum of two acquisitions are necessary: (i) for $b_0 = 0$ s.mm^{-2} where the measured signal is equal to S_0, and (ii) $b_1 > 0$ s.mm^{-2} (typically 1000 s.mm^{-2}). Then, the ADC map can be computed as:

$$\text{ADC} = -\frac{\ln\left(\dfrac{S(b_1)}{S_0}\right)}{b_1} \ . \tag{2.6}$$

More accurate computation of the ADC map can be obtained by performing several acquisitions with different values for the parameter b and performing a semi-logarithmic linear fitting using the model presented in Eq. (2.5).

Regarding the appearance of the ADC maps, it was previously stated that by increasing the value of b, the signal of CaP tissue increases significantly. From Eq. (2.6), it can be shown that tissue appearance in the ADC map will be the inverse of DW MRI images. Then, CaP tissue is associated with low-SI whereas healthy tissue appears brighter as depicted in Fig. 2.4(b) (34).

Similar to the gain achieved by DW MRI, diagnosis using ADC map combined with T_2-W MRI significantly outperforms T_2-W MRI alone (4, 100). Moreover, it has been shown that ADC is correlated with GS (101, 102, 103).

However, some tissues of the CG zone mimic CaP with low-SI (68) and image distortion can arise due to haemorrhage (4). It has also been noted that a high variability of the ADC occurs between different patients making it difficult to define a static threshold to distinguish CaP from non-malignant tumours (4).

2.2.6 MRSI

CaP induces metabolic changes in the prostate compared with healthy tissue. Thus, CaP detection can be carried out by tracking changes of metabolite concentration in prostate tissue. MRSI is an NMR-based technique which generates spectra of relative metabolite concentration in a ROI.

In order to track changes of metabolite concentration, it is important to know which metabolites are associated with CaP. To address this question, clinical studies identified

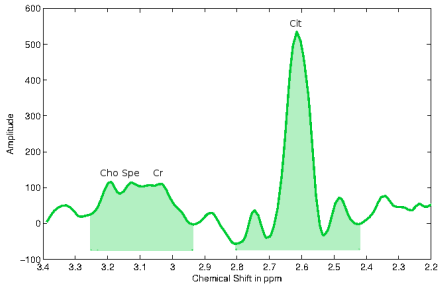

(a) Illustration of an MRSI spectrum of an healthy voxel acquired with a 3.0 Tesla MRI.

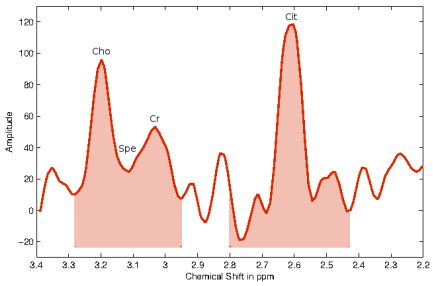

(b) Illustration of an MRSI spectrum of a cancerous voxel acquired with a 3.0 Tesla MRI.

Figure 2.5: Illustration of an MRSI spectrum both healthy and cancerous voxel with a 3.0 Tesla MRI. The highlighted areas corresponds to the related concentration of the metabolites which is computed by integrating the area under each peak. Acronyms: Choline (Cho), Spermine (Spe), Creatine (Cr) and Citrate (Cit).

three biological markers: (i) citrate, (ii) choline and (iii) polyamines composed mainly of spermine, and in less abundance of spermidine and putrescine (104, 105, 106).

Citrate is involved in the production and secretion of the prostatic fluid, and the glandular prostate cells are associated with a high production of citrate enabled by zinc accumulation by these same cells (105). However, the metabolism allowing the accumulation of citrate requires a large amount of energy (105). In contrast, malignant cells do not have high zinc levels leading to lower citrate levels due to citrate oxydation (105). Furthermore, this change results in a more energy-efficient metabolism enabling malignant cells to grow and spread (105).

An increased concentration of choline is related to CaP (104). Malignant cell development requires epigenetic mechanisms resulting in metabolic changes and relies on two mechanisms: DNA methylation and phospholid metabolism which both result in choline uptake, explaining its increased level in CaP tissue (104). Spermine is also considered as a biological marker in CaP (106, 107). In CaP, reduction of the ductal volume due to shifts in polyamine homeostasis might lead to a reduced spermine concentration (107).

To determine the concentration of these biological markers, one has to focus on the MRSI modality. In theory, in presence of a homogeneous magnetic field, identical nuclei precesses at the same operating frequency known as the Lamor frequency (108). However, MRSI is based on the fact that identical nuclei will slightly precess at different

frequencies depending on the chemical environment in which they are immersed (108), a phenomenon known as the chemical shift effect (CSE) (6). Given this property, metabolites can be identified and their concentrations can be determined. In this regard, the Fourier transform is used to obtain the frequency spectrum of the NMR signal (6, 108). In this spectrum, each peak is associated with a particular metabolite and the area under each peak corresponds to the relative concentration of this metabolite (see Fig. 2.5) (6).

Two different quantitative approaches are used to decide or whether not the spectra of a ROI is associated with CaP classified either as relative quantification or absolute quantification (109). In relative quantification, the ratio of choline-polyamines-creatine to citrate is computed. The integral of the signal is computed from choline (cf., 3.21 ppm) to creatine (cf., 3.02 ppm) because the peaks in this region can be merged at clinical magnetic field strengths (see Fig. 2.5) (33, 107). Considering the previous assumption that choline concentration rises and citrate concentration decreases in the presence of CaP, the ratio computed should be higher in malignant tissue than in healthy tissue.

Two different quantitative approaches are used to decide or not the spectra of a ROI is associated with CaP classified either as relative quantification or absolute quantification (109). In relative quantification, the ratio of choline-polyamines-creatine to citrate is computed. The integral of the signal is computed from choline (cf., 3.21 ppm) to creatine (cf., 3.02 ppm) because the peaks in this region can be merged at clinical magnetic field strengths (see Fig. 2.5) (33, 107). Considering the previous assumption that choline concentration rises and citrate concentration decreases in the presence of CaP, the ratio computed should be higher in malignant tissue than in healthy tissue.

In contrast with relative quantification, absolute quantification measures molar concentrations by normalizing relative concentrations using water as reference (109). In this case, "true" concentrations are directly used to differentiate malignant from healthy tissue. However, this method is not commonly used as it requires an additional step of acquiring water signals, inducing time and cost acquisition constraints.

MRSI allows examination with high specificity and sensitivity compared to other MRI modalities (4). Furthermore, it has been shown that combining MRSI with MRI improves detection and diagnosis performance (110, 111, 112). Citrate and spermine concentrations are inversely correlated with the GS allowing us to distinguish low from high grade CaPs (106). However, choline concentration does not provide the same properties (106).

Unfortunately, MRSI also presents several drawbacks. First, MRSI acquisition is time consuming which prevents this modality from being used in daily clinical practise (34). In addition, MRSI suffers from low spatial resolution due to the fact that signal-to-noise (SNR) is linked to the voxel size. However, this issue is addressed by developing new scanners with higher magnetic field strengths such as 7.5 T (106). Finally, a high variability of the relative concentrations between patients was observed (4). The same observation was made depending on the zones studied (cf., PZ, CG, base, mid-gland, apex) (109, 113). Due to this variability, it is difficult to use a fixed thresholds in order to differentiate CaP from healthy tissue.

Chapter 3

Review of CADe and CADx for CaP

As previously mentioned in the introduction (see Sect. 1.4), CADs are developed to advise and backup radiologists in their tasks of CaP detection and diagnosis, but not to provide fully automatic decisions (53). CADs can be divided into two different subgroups either as CADe, with the purpose to highlight probable lesions in MRI images, or CADx, which focuses on differentiating malignant from non-malignant tumours (53). Moreover, an intuitive approach, motivated by developing a framework combining detection-diagnosis, is to mix both CADe and CADx by using the output of the former mentioned as a input of the latter named. Although the outcomes of these two systems should differ, the framework of both CAD systems is similar. A general CAD work-flow is presented n Fig. 2.1.

MRI modalities mentioned in Sect. **??** are used as inputs of CAD for CaP. These images acquired from the different modalities show a large variability between patients: the prostate organ can be located at different positions in images (e.g., patient motion, variation of acquisition plan), and the SI can be corrupted with noise or artefacts during the acquisition process (eg., magnetic field inhomogeneity, use of endorectal coil). To address these issues, the first stage of CAD is to pre-process multiparametric MRI images to reduce noise, remove artefacts and standardize the SI. At most of the later processes will be only focused on the prostate, it is necessary to segment the prostate in each MRI-modality to define it as a ROI. However, data may suffer from misalignment due to patient motions or different acquisition parameters. Therefore, a registration step

is usually performed so that all the previously segmented MRI images will be in the same reference frame. Registration and segmentation can be swapped depending on the strategy chosen.

Some studies do not fully apply the methodology depicted in Fig.. 2.1. Details about those can be found in Tab. 3.1. Some studies proposed methods in which inputs are the MRI raw data inorder to demostrate the robustness of their approaches to noise or artefacts. In some cases, prostate segmentation is performed manually as well as registration. It is also sometimes assumed that no patient motions occur during the acquisition procedure, removing the need of registering the multiparametric MRI images.

Once the data are regularized, it becomes possible to extract features and classify the data to obtain either the location of possible lesions (CADe) or/and the malignancy nature of these lesions (CADx).

In a CADe framework, *possible lesions will be segmented automatically* and further used as input of CADx. Nevertheless, some works also used a fusion CADe-CADx framework in which a voxel-based features are directly used, allowing to obtain the location of the malignant lesions as results. On the other hand, manual lesions segmentation are not considered to be part of CADe. The output of the CADe is used as input of the CADx.

CADx is composed of the processes allowing to *distinguish malignant from non-malignant tumours*. Here, CaP malignancy is defined using the grade of the GS determined after post biopsy or prostatecomy. As presented in Fig.. 2.1, CADx is usually composed of the three common steps used in classification framework: (i) features detection, (ii) feature extraction/selection and (iii) feature classification.

3.1 Literature classification

This section is organized using the methodology presented in Fig.. 2.1. Methods embedded in the image regularization framework are presented initially to subsequently focus on the image classification framework, being divided into CADe and CADx. Table 3.1 summarizes the fourty-two different CAD studies reviewed in section. The first set of information reported is linked to the data acquisition such as the number of patients included in the study, the modalities acquired as well as the strength of the field of the scanner used. Subsequently, information about the prostate zones considered in the

CAD analysis (PZ or CG) are reported since that detecting CaP in the CG is a more challenging problem and has received particular attention only in the recent publications.

Table 3.1: Overview of the different studies reviewed with their main characteristics. Acronyms: number (#) - image regularization (Img. Reg.).

Index	Study	# patients	MRI-modality				Strength of field		Studied zones		CAD stages		
			T_2-W MRI	DCE MRI	DW MRI	MRSI	1.5 T	3.0 T	PZ	CG	Img. Reg.	CADe	CADx
[1]	(114)	25	✓	✓	✗	✗	✓	✗	✓	✗	✓!	✗	✓
[2]	(115)	25	✓	✓	✗	✗	✓	✗	✓	✗	✓!	✗	✓
[3]	(116)	53	✓	✗	✓	✗	✓	✗	✓	✓	✗	✗	✓
[4]	(117)	10	✓	✓	✓	✗	✓	✗	✓	✗	✗	✓	✓
[5]	(118)	21	✓	✓	✓	✗	✓	✗	✓	✗	✓!	✓	✓
[6]	(119)	15	✓	✗	✓	✗	✓	✗	✓	✗	✗	✗	✓
[7]	(120)	10	✓	✓	✓	✗	✓	✗	✓	✗	✓	✓	✓
[8]	(121)	24	✗	✗	✗	✓	✓	✗	✓	✓	✓!	✓	✓
[9]	(122)	25	✓	✓	✓	✗	✓	✗	✓	✗	✓!	✗	✓
[10]	(123)	188	✓	✓	✓	✗	✗	✓	✓	✗	✓!	✓	✓
[11]	(124)	288	✓	✓	✓	✗	✗	✓	✓	✓	✓!	✓	✓
[12]	(125)	11	✓	✓	✓	✗	✓	✗	✓	✗	✓!	✓	✓
[13]	(126)	54	✓	✓	✓	✗	✗	✓	✓	✓	✓!	✗	✓
[14]	(127)	27	✓	✗	✗	✗	✓	✗	✓	✗	✓!	✓	✓
[15]	(128)	55	✓	✗	✗	✗	✓	✗	✓	✗	✓!	✗	✓
[16]	(129)	18	✗	✗	✗	✓	✗	✓	✓	✓	✗	✓	✓
[17]	(130)	10	✗	✓	✗	✗	✓	✗	✓	✗	✓!	✓	✓
[18]	(2)	23	✓	✓	✓	✗	✓	✗	✓	✗	✓!	✗	✓
[19]	(3)	30	✓	✓	✓	✗	✓	✗	✓	✗	✓!	✗	✓
[20]	(131)	20	✓	✓	✓	✗	✓	✗	✓	✗	✓!	✓	✓
[21]	(132)	20	✓	✓	✓	✗	✓	✗	✓	✗	✓!	✓	✓
[22]	(133)	22	✗	✗	✗	✓	✗	✓	✓	✓	✓!	✓	✓
[23]	(103)	48	✓	✓	✓	✗	✗	✓	✓	✓	✗	✗	✓
[24]	(134)	100	✗	✓	✗	✗	✓	✗	✓	✓	✗	✗	✓
[25]	(135)	42	✗	✓	✗	✗	✗	✓	✓	✓	✗	✓	✓
[26]	(136)	14	✗	✗	✗	✓	✓	✗	✓	✓	✓!	✓	✓
[27]	(137)	18	✗	✗	✗	✓	✓	✗	✓	✓	✓!	✓	✓
[28]	(138)	18	✗	✗	✗	✓	✓	✗	✓	✓	✓!	✓	✓
[29]	(139)	15	✓	✗	✗	✓	✓	✗	✓	✓	✓!	✓	✓
[30]	(140)	19	✓	✗	✗	✓	✓	✗	✓	✓	✓!	✓	✓
[31]	(141)	36	✓	✗	✗	✓	✓	✗	✓	✓	✗	✓	✓
[32]	(142)	29	✓	✗	✗	✓	✓	✗	✓	✓	✓!	✓	✓
[33]	(143)	16	✓	✗	✗	✓	✓	✗	✓	✓	✗	✓	✓
[34]	(144)	6	✓	✓	✗	✗	✗	✓	✓	✓	✓!	✓	✓
[35]	(145)	6	✓	✓	✗	✗	✗	✓	✓	✓	✓	✓	✓
[36]	(146)	12	✓	✓	✓	✗	✗	✓	✓	✓	✓!	✓	✓
[37]	(147)	22	✓	✗	✗	✗	✗	✓	✓	✓	✓	✓	✓
[38]	(148)	29	✓	✓	✗	✗	✓	✗	✓	✗	✓!	✗	✓
[39]	(149)	29	✗	✓	✗	✗	✓	✗	✓	✗	✓!	✗	✓
[40]	(150)	29	✓	✓	✗	✗	✓	✗	✓	✗	✓!	✗	✓
[41]	(151)	NA	✓	✓	✓	✗	✗	✓	✓	✗	✓!	✓	✓

Notes:
✗: not used or not implemented.
✓!: partially implemented.
✓: used or implemented.

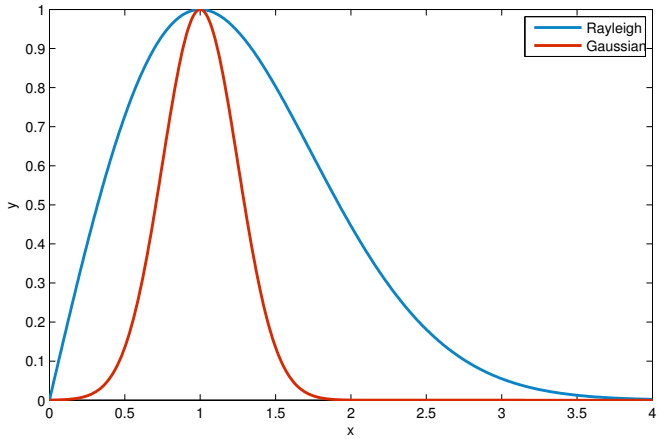

Figure 3.1: Illustration of a Gaussian distribution ($\mu = 1, \sigma = 0.25$) and a Rayleigh distribution ($\sigma = 2$). It can be seen that the Rayleigh distribution is suffering of a bias term when compared with the Gaussian distribution.

3.1.1 Image regularization framework

This section provides a review of the methods used in CADs for CaP in order to regularize input images. We start with pre-processing methods presented in Sect.. 3.1.1.1, focusing mainly on the reduction of noise level and artefacts as well as standardization of SI. Sections 3.1.1.2 and **??** will be dedicated to segmentation methods, so that later methods only operate on the segmented prostate, and registration to align segmented images from different MRI-modalities in the same reference frame.

3.1.1.1 Pre-processing

Three different groups of pre-processing methods are commonly applied to images as initial stage in CAD for CaP. These methods are explained for both MRI and MRSI modalities, while a summary of the applied methods in CAD is presented in Table. 3.2.

– ***Noise filtering:*** The NMR signal measured and recorded in the k-space during an MRI acquisition is affected by noise. This noise obeys a complex Gaussian white noise mainly due to thermal noises in the patient area (152). Furthermore, MRI images visualized by radiologists are in fact the magnitude images resulting from the complex Fourier transform of the k-space data. The complex Fourier transform, being a linear and orthogonal transform, does not affect the Gaussian noise characteristics (152). However, the function involved in the magnitude computation is a non-linear transform (i.e., the square root of the sum of squares of real and the imaginary parts), implying that the noise distribution is no longer Gaussian; it indeed follows a Rician distribution making the denoising task harder. Briefly, a Rician distribution can be characterized as follows: in low-SI region (low SNR), it can be approximated with a

Rayleigh distribution while in high-SI region (high SNR), it is similar to a Gaussian distribution (see Fig. 3.1) (153). Reviews of all denoising methods can be found in (154, 155).

Median filtering is the simplest approach used to address the denoising issue in MRI images (131, 132). In both studies, Ozer *et al.* used a square kernel of size 5×5 pixels with the image resolutions ranging from 320×256 (cf., T_2-W MRI) to 256×128 (cf., T_2 map, DCE and DW MRI) and a field of view (FOV) ranging from 14 cm (cf, T_2-W and DW MRI) to 20 cm (cf, T_2 map and DCE MRI). However, from a theoretical point of view, this simple filtering method is not well formalized to address the noise distribution in MRI images.

More complex approaches were proposed to overcome this problem. A common method used to denoise MRI images is based on wavelet-based filtering. This filtering exploits the sparsity property of the wavelet decomposition. The projection of a noisy signal from the spatial-domain to the wavelet-domain implies that only few wavelet coefficients contribute to the "signal-free noise" while all wavelet coefficients contribute to the noise (156). Therefore, denoising is performed by thresholding/attenuating the insignificant wavelet coefficients to enforce the sparsity in the wavelet-domain. Investigations focus on the strategies to perform the most adequate coefficient shrinkage method (e.g., using thresholding, singularity property or Bayesian framework) (157).

Ampeliotis *et al.* in (114, 115) performed wavelet shrinkage to denoise magnitude MRI images (cf., T_2-W-MRI and DCE-MRI) using thresholding techniques (158). However, since the wavelet transform is an orthogonal transform, the Rician distribution of the noise is preserved in the wavelet-domain. Hence, for low SNR, the wavelet and scaling coefficients still suffer from a bias due to this specific noise distribution (152).

Lopes *et al.* in (127) used the filtering technique proposed by (159) to denoise T_2-W-MRI which was based on joint detection and estimation theory (159). In this approach, the wavelet coefficients "free-of-noise" are estimated from the noisy wavelet coefficients using a maximum *a posteriori* (MAP) estimate. Furthermore, the estimator designed takes spatial context into account by including both local and global information in the prior probabilities. The different probabilities needed by the MAP are empirically estimated by using mask images representing the locations of the significant wavelet coefficients. These mask images are computed by thresholding the detail images obtained from the wavelet decomposition. To remove the bias from the wavelet and scaling coefficients, the squared magnitude MRI image used instead of the magnitude MRI image as proposed by (152). This involves changing the Rician distribution to a scaled non-central Chi-square distribution. It implies that the wavelet coefficients are also unbiased estimators and the scaling coefficients are unbiased estimators but up to a constant C as defined in Eq. (3.1) which needs to be subtracted from each scaling coefficient,

$$C = 2^{(J+1)}\hat{\sigma}^2 \ , \tag{3.1}$$

where J is the number of levels of the wavelet decomposition and $\hat{\sigma}$ is an estimate of

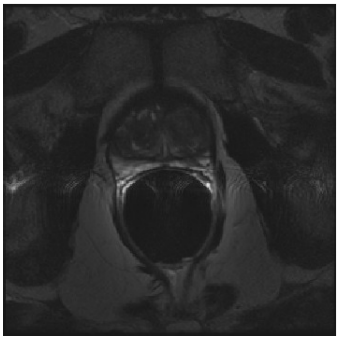

Figure 3.2: Example of artefacts with high SI due to perturbation from the endorectal coil which create inhomogeneity.

the noise standard deviation.

– ***Bias correction:*** Besides being corrupted by noise, MRI images are also affected by the inhomogeneity of the MRI field commonly referred to as bias field (160). This bias field results in a smooth variation of the SI through the image. When an endorectal coil is used, an artefact resulting of an hyper-intense signal can be observed around the coil on the images (see Fig. 3.2).

As a consequence, the SI of identical tissues varies depending on their spatial location in the image making further processes such as segmentation or registration harder (161, 162). A review of bias correction methods can be found in (162).

The model of image formation is usually formalized such that:

$$s(\mathbf{x}) = o(\mathbf{x})b(\mathbf{x}) + \eta(\mathbf{x}) \ , \tag{3.2}$$

where $s(\mathbf{x})$ is the corrupted SI at the pixel for the image coordinates $\mathbf{x} = \{x, y\}$, $o(\mathbf{x})$ is the "noise-free signal" , $b(\mathbf{x})$ is the bias field function and $\eta(\mathbf{x})$ is an additive white Gaussian noise.

Hence, the task of bias correction involves estimating the bias function $b(\mathbf{x})$ in order to infer the "signal-free bias" $o(\mathbf{x})$.

Viswanath *et al.* (145) performed bias correction on T_2-W-MRI using a parametric Legendre polynomial model proposed in (160) and available in the Insight Segmentation and Registration Toolkit (ITK) library[1].

Styner *et al.* (160) chose to model the bias field by using a linear combination of Legendre polynomials as:

$$\hat{b}(\mathbf{x}, \mathbf{p}) = \sum_{i=0}^{m-1} p_i f_i(\mathbf{x}) = \sum_{i=0}^{l} \sum_{j=0}^{l-i} p_{ij} P_i(x) P_j(y) \ , \tag{3.3}$$

where $\hat{b}$ is the bias estimation with the image coordinates $\mathbf{x} = \{x, y\}$ and the m

[1]The ITK library is available at: `http://www.itk.org/`

coefficients of the linear combination $\mathbf{p} = p_{11}, \ldots, p_{ij}$; m can be defined as $m = (l+1)\frac{(l+2)}{2}$ where l is the degree of Legendre polynomials chosen and $P_i(\cdot)$ denotes a Legendre polynomial of degree i.

This family of functions allows us to model the bias as a smooth inhomogeneity function across the image. To estimate the set of parameters $\mathbf{p}$, a cost function is defined which relies on the following assumptions: (i) an image is composed of k regions with μ_k being the mean SI and a variance σ_k^2 of each particular class, and (ii) each noisy pixel belongs to one of the k regions with its SI value close to the class mean μ_k. Hence, the cost function is defined as:

$$C(\mathbf{p}) = \sum_{\mathbf{x}} \prod_{k} \rho_k(s(\mathbf{x}) - \hat{b}(\mathbf{x}, \mathbf{p}) - \mu_k) \ , \tag{3.4}$$

$$\rho_k(x) = \frac{x^2}{x^2 + 3\sigma_k^2} \ , \tag{3.5}$$

where $\rho_k(\cdot)$ is a M-estimator allowing estimations to be less sensitive to outliers than usual square distance (163).

Finally, estimation of the parameters $\mathbf{p}$ results in finding the minimum of the cost function $C(\mathbf{p})$. This optimization was performed using the non-linear $(1+1)$ Evolution Strategy (ES) optimizer (164).

In a later publication, (147) make use of the well known N3 algorithm[1] to correct T_2-W-MRI developed by (165). To estimate the bias function, (165) proposed to estimate the probability density functions (PDFs) of the signal and bias.

Recalling Eq. (3.2) and taking advantage of logarithm property, it implies that this model becomes additive such that:

$$\begin{aligned} \log s(\mathbf{x}) &= \log b(\mathbf{x}) + \log\left(o(\mathbf{x}) + \frac{\eta(\mathbf{x})}{b(\mathbf{x})}\right) \ , \\ &\approx \log b(\mathbf{x}) + \log \hat{o}(\mathbf{x}) \ , \end{aligned} \tag{3.6}$$

where $\hat{o}(\mathbf{x})$ is the signal only degraded by noise. (165) shows that Eq. (3.6) can be related to PDFs such that:

$$S(s) = B(s) * O(s) \ , \tag{3.7}$$

where S, B and O are respectively the probability densities of s, b and o.

Restoring the corrupted signal s is carried out by finding the multiplicative field b which maximizes the frequency content of the distribution O. Sled *et al.* (165) argue that a search through all possible fields b and selection of the one which maximizes the high frequency content of O could be carried out but results in an exhaustive search. However, they show that the bias field distribution can be assimilated to a near Gaussian distribution. Using this fact as *a priori*, it is then possible to infer

[1]The N3 algorithm implementation is available at: `http://www.bic.mni.mcgill.ca/software/N3/`

the distribution O using Wiener deconvolution given B and S and later estimate the corresponding smooth field b.

Lv *et al.* (128) corrected the inhomogeneity in T_2-W-MRI images by using the method proposed in (166). In this method, the MRI images are corrected iteratively by successively detecting the image foreground via generalized scale (g-scale) and estimating a bias field function based on a second-order polynomial model. First the background of the MRI image is eliminated by threholding. The threshold value is commonly equal to the mean SI of the considered image. Then, in the seeded region growing algorithm is applied considering every thresholded pixel as a potential seed. However, pixels already assigned to a region will not be considered any more as seed. As in seeded region growing algorithm (167), two criteria are taken into account to expand the region. First, the region will grow using a connected-neighbourhood, initially defined by the user. Then, the homogeneity of SI is based on a fuzzy membership function taking into account the absolute difference of the SIs of two pixels. Depending on the membership value (cf., a threshold has to be defined), the pixel considered is merged or not to the region. Once this segmentation is performed, the largest region R is used as a mask to select pixels of the original image and the mean SI, μ_R, is computed. The background variation $b(\mathbf{x})$ is estimated as:

$$b(\mathbf{x}) = \frac{s(\mathbf{x})}{\mu_R}, \ \forall \mathbf{x} \in R \ , \tag{3.8}$$

where $s(\mathbf{x})$ is the original MRI image.

Finally, a second order polynomial $\hat{b}_\Theta(\mathbf{x})$ is fitted in a least-squares sense (Eq. (3.9)),

$$\hat{\Theta} = \arg\min_{\Theta} |b(\mathbf{x}) - \hat{b}_\Theta(\mathbf{x})|^2, \ \forall \mathbf{x} \in R \ . \tag{3.9}$$

Finally, the whole original MRI image is corrected by dividing it by the estimated bias field function $\hat{b}_\Theta(\mathbf{x})$. This process is repeated until the number of pixels in the largest region R does not change significantly between two iterations.

– ***SI normalization/standardization:***

As discussed in the later section, segmentation or classification tasks are usually performed by first learning from a training set of patients. Hence, one can emphasize the desire to perform MRI examinations with a high repeatability or in other words, one would ensure to obtain similar MRI images (cf., similar SIs) for patients of the same group (cf., healthy patients *vs.* patients with CaP), for a similar sequence.

However, it is a known fact that variability between patients occurs during the MRI examinations even using the same scanner, protocol or sequence parameters (168). Hence, the aim of normalization or standardization of the MRI data is to remove the variability between patients and enforce the repeatability of the MRI examinations. Approaches used to standardize MRI images can be either categorized as statistical-based standardization or organ SI-based standardization.

Artan *et al.* (117, 118) as well as Ozer *et al.* (131, 132) standardized T_2-W, DCE and DW MRI images by computing the *standard score* (also called *z-score*) of the

pixels of the PZ as:

$$I_s(\mathbf{x}) = \frac{I_r(\mathbf{x}) - \mu_{pz}}{\sigma_{pz}},\ \forall \mathbf{x} \in \text{PZ}\ , \tag{3.10}$$

where $I_s(\mathbf{x})$ is the standardized SI with the image coordinates $\mathbf{x} = \{x, y\}$, $I_r(\mathbf{x})$ is the raw SI, mu_{pz} is the mean-SI of the PZ and σ_{pz} is the SI standard deviation in the PZ. This transformation enforces the image PDF to have a zero mean and a unit standard deviation.

In a similar way, Liu *et al.* (126) normalized T_2-W-MRI by making use of the median and interquartile range for all the pixels.

Lv *et al.* (128) scaled the SI of T_2-W-MRI images using the method proposed in (1) based on PDF matching. This approach is based on the assumption that MRI images from the same sequence should share the same PDF appearance. Hence, one can approach this issue by transforming and matching the PDFs using some statistical landmarks such as median and different quantiles. Using a training set, these statistical landmarks are extracted for N training images as for instance for the minimum, the 25^{th} quantile, the median, the 75^{th} quantile and the maximum:

$$\begin{aligned}
\Phi_0 &= \{\phi_0^1, \phi_0^2, \cdots, \phi_0^N\}\ , \\
\Phi_{25} &= \{\phi_{25}^1, \phi_{25}^2, \cdots, \phi_{25}^N\}\ , \\
\Phi_{50} &= \{\phi_{50}^1, \phi_{50}^2, \cdots, \phi_{50}^N\}\ , \\
\Phi_{75} &= \{\phi_{75}^1, \phi_{75}^2, \cdots, \phi_{75}^N\}\ , \\
\Phi_{100} &= \{\phi_{100}^1, \phi_{100}^2, \cdots, \phi_{100}^N\}\ ,
\end{aligned} \tag{3.11}$$

where $\phi_{n^{\text{th}}}^{i^{\text{th}}}$ is the n^{th} quantile of the i^{th} training image.

Then, the mean of each quantile $\{\bar{\Phi}_0, \bar{\Phi}_{25}, \bar{\Phi}_{50}, \bar{\Phi}_{75}, \bar{\Phi}_{100}\}$ is also calculated. Once this training stage is performed, a linear transformation by parts $\mathcal{T}(\cdot)$ can be computed (Eq. (3.12)) for each test image t by mapping each statistical landmark ${\varphi_{(cdot)}}^t$ of this image with the pre-learned statistical landmarks $\bar{\Phi}_{(\cdot)}$. This linear mapping is also depicted in Fig. 3.3.

$$\mathcal{T}(s(\mathbf{x})) = \begin{cases}
\lceil \bar{\Phi}_0 + (s(\mathbf{x}) - \varphi_0^t)\left(\frac{\bar{\Phi}_{25} - \bar{\Phi}_0}{\varphi_{25}^t - \varphi_0^t}\right) \rceil\ , & \text{if } \varphi_0^t \leq s(\mathbf{x}) < \varphi_{25}^t)\ , \\
\lceil \bar{\Phi}_{25} + (s(\mathbf{x}) - \varphi_{25}^t)\left(\frac{\bar{\Phi}_{50} - \bar{\Phi}_{25}}{\varphi_{50}^t - \varphi_{25}^t}\right) \rceil\ , & \text{if } \varphi_{25}^t \leq s(\mathbf{x}) < \varphi_{50}^t)\ , \\
\lceil \bar{\Phi}_{50} + (s(\mathbf{x}) - \varphi_{50}^t)\left(\frac{\bar{\Phi}_{75} - \bar{\Phi}_{50}}{\varphi_{75}^t - \varphi_{50}^t}\right) \rceil\ , & \text{if } \varphi_{50}^t \leq s(\mathbf{x}) < \varphi_{75}^t)\ , \\
\lceil \bar{\Phi}_{75} + (s(\mathbf{x}) - \varphi_{75}^t)\left(\frac{\bar{\Phi}_{100} - \bar{\Phi}_{75}}{\varphi_{100}^t - \varphi_{75}^t}\right) \rceil\ , & \text{if } \varphi_{75}^t \leq s(\mathbf{x}) \leq \varphi_{100}^t)\ ,
\end{cases} \tag{3.12}$$

Viswanath *et al.* (145, 146, 147) use a variant of this previous approach presented in (169) aiming to standardize the T_2-W-MRI images.Instead of computing the PDF of an entire image, a pre-segmentation of the foreground is carried out via g-scale which was discussed in the bias correction section. Once the foreground is detected,

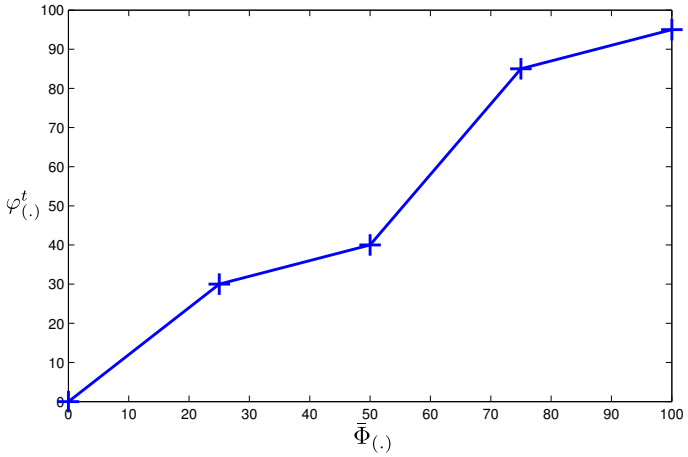

Figure 3.3: Example of linear mapping by parts as proposed by (1).

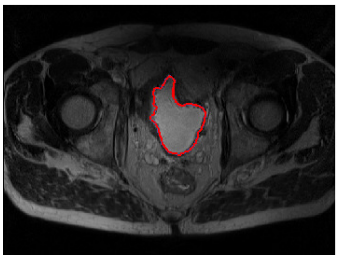

(a) Illustration and location of the bladder on a T_2-W-MRI image acquired with a 3.0 Tesla MRI scanner

(b) Illustration and location of the femoral arteries on a T_1-W-MRI image acquired with a 3.0 Tesla MRI scanner

Figure 3.4: Illustration of the two organs used by (2, 3) to normalize T_2-W and T_1-W MRI images.

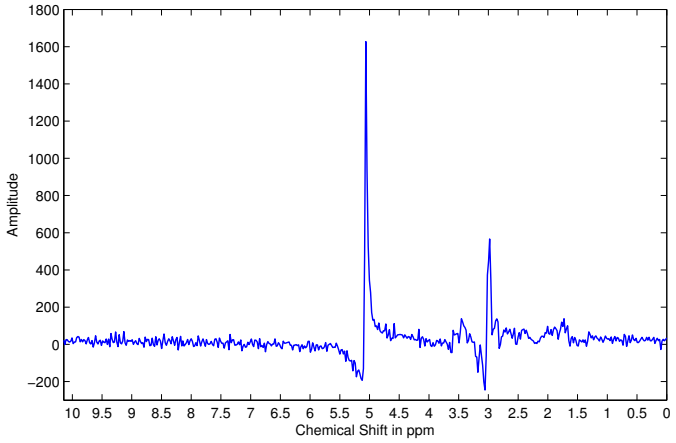

Figure 3.5: Illustration of phase misalignment in an MRSI spectra acquire with a 3.0 Tesla MRSI scanner. Note the distortion of the signal specially visible for the water and citrate peaks.

the largest region is extracted and the same process than previously mentioned (see Eq. (3.12)) takes place in order to align PDFs of the foreground of the MRI images.

The methods described above were statistical-based methods. However, the standardization problem can be tackled by normalizing the MRI images using the SI of some known organs present in these images. Niaf *et al.* (2, 3) normalized T_2-W-MRI images by dividing the original SI of the images by the mean SI of the bladder (see Fig. 3.4(a)). Likewise, (2) standardized the T_1-W-MRI images using the arterial input function (AIF). They computed the AIF by taking the mean of the SI in the most enhanced part of the common femoral arteries (see Fig. 3.4(b)) as proposed in (170).

Presented in Sect. 2.2.6, MRSI is a modality related to a one dimensional signal. Hence, specific pre-processing steps for this type of signals have been applied instead of standard signal processing methods.

– ***Phase correction:*** MRSI data acquired suffer from zero-order and first-order phase misalignments as shown in Fig. 3.5 (171, 172). Parfait *et al.* (133) used a method proposed in (171) where the phase of MRSI signal is corrected based on entropy minimization in the frequency domain. The corrected MRSI signal $o(\xi)$ can be expressed as:

$$\begin{aligned} \Re(o(\xi)) &= \Re(s(\xi))\cos(\Phi(\xi)) - \Im(\xi)\sin(\Phi(\xi)) \ , \\ \Im(o(\xi)) &= \Im(s(\xi))\cos(\Phi(\xi)) + \Re(\xi)\sin(\Phi(\xi)) \ , \\ \Phi(\xi) &= \phi_0 + \phi_1 \frac{\xi}{N} \ , \end{aligned} \tag{3.13}$$

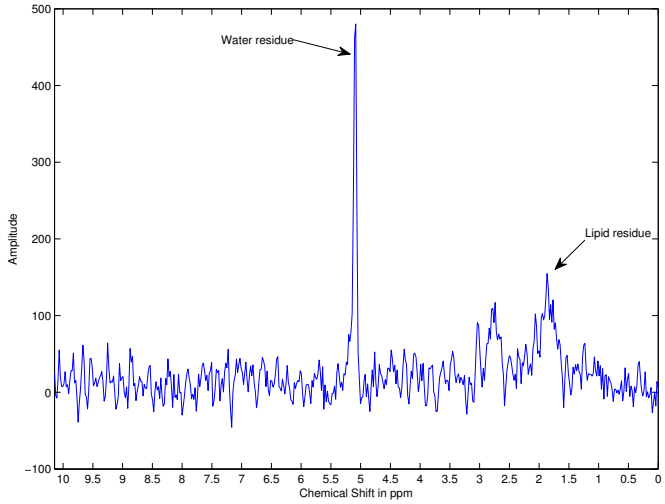

Figure 3.6: Illustration of the residues of water and fat even after their suppression during the acquisition protocol. The acquisition was carried out with a 3.0 Tesla MRI.

where $\Re(\cdot)$ and $\Im(\cdot)$ are the real and imaginary part of the complex signal respectively, $s(\xi)$ is the corrupted MRSI signal, ϕ_0 and ϕ_1 are the zero-order and first-order phase correction terms respectively and N is the total number of samples of the MRSI signal.

Chen *et al.* (171) tackled this problem using an optimization framework where ϕ_0 and ϕ_1 had to be inferred. Hence, the simplex Nelder-Mead optimization method was used to minimize the following cost function based on the *Shannon entropy* formulation:

$$\hat{\Phi} = \arg\min_{\Phi} \left[-\sum \Re(s'(\xi)) \ln \Re(s'(\xi)) + \lambda \|\Re(s(\xi))\|_2 \right] , \tag{3.14}$$

where $s'(\xi)$ is the first derivative of the corrupted signal $s(\xi)$ and λ is a regularization parameter. Once the best parameter Φ is obtained, the MRSI signal is corrected using Eq. (3.13).

– ***Water and lipid residuals filtering:*** The water and lipid metabolites occur in much higher concentrations the metabolites of interests (cf., choline, creatine and citrate) (172, 173). Fortunately, specific MRSI sequences were developed in order to suppress water and lipid metabolites using pre-saturation techniques (173). However, these techniques do not perfectly remove water and lipids peaks and some residuals are still present in the MRSI spectra as shown in Fig. 3.6. Therefore, different post-processing methods have been proposed to enhance the quality of the MRSI spectra by removing these residuals. For instance, Kelm *et al.* (121) used the well known HSVD algorithm proposed by (174) which models the MRSI signal by a sum of exponentially

damped sinusoids in the time domain (see Eq. (3.15)).

$$s(t) = \sum_{k=1}^{K} a_k \exp(i\phi_k) \exp(-d_k + i2\pi f_k)t + \eta(t) \ , \tag{3.15}$$

where a_k is the amplitude proportional to the metabolite concentration with a resonance frequency f_k, d_k represents the damping factor of the exponential, ϕ_k is the first-order phase and $\eta(t)$ is a complex white noise.

Pijnappel *et al.* (174) showed that the "noise-free signal" can be found using the singular value decomposition (SVD) decomposition. First the noisy signal is reorganized inside a Hankel matrix H. It can be shown that if the signal considered would be a "noise-free signal", the rank of H would be equal to rank K. However, due to the presence of noise, H is in fact a full rank matrix. Thus, to recover the "noise-free signal", the rank of H can be truncated to K using its SVD decomposition. Hence, knowing the cut off frequencies of water (cf., 4.7 ppm) and lipid (cf., 2.2 ppm) metabolites, their corresponding peaks can be reconstructed and subtracted from the original signal (175).

– ***Baseline correction:*** Sometimes, the problem discussed in the above section regarding the lipid molecules is not addressed simultaneously with water residuals suppression. Lipids and macromolecules are known to affect the baseline of the MRSI spectra. They could cause errors during further fitting processes aiming to quantify the metabolites, especially regarding the citrate metabolite.

Parfait *et al.* (133) made the comparison of two different methods to detect the baseline and correct the MRSI spectra which are based on (176, 177). Lieber *et al.* (176) addressed the problem of baseline detection in the frequency domain by fitting a low degree polynomial whereas Parfait *et al.* (133) modified this algorithm by convolvinga Gaussian kernel to smooth the MRSI signal instead of fitting a polynomial function. **Check the tex file to see the commented area pre-processing.tex**

Unlike in (176), Devos *et al.* (177) proposed to correct the baseline in the time domain by multiplying the MRSI signal by a decreasing exponential function as:

$$c(t) = \exp(-\beta t) \ , \tag{3.16}$$

Having a typical value for β of 0.15. However, Parfait *et al.* (133) concluded that the method proposed in (176) outperformed the one in (177).

In the contemporary work of Tiwari *et al.* (141), the authors detected the baseline using a local non-linear fitting method avoiding regions with significant peaks which were detected using a experimentally parametrised signal-to-noise ratio (i.e. a value larger than 5 dB).

– ***Frequency alignment:*** Due to variations of the experimental conditions, a frequency shift can be observed in the MRSI spectra (171, 172) as shown in Fig. 3.7.

Tiwari *et al.* (141) corrected the frequency shift by first detecting known metabolite peaks such as choline, creatine and citrate. The frequency shift is corrected by

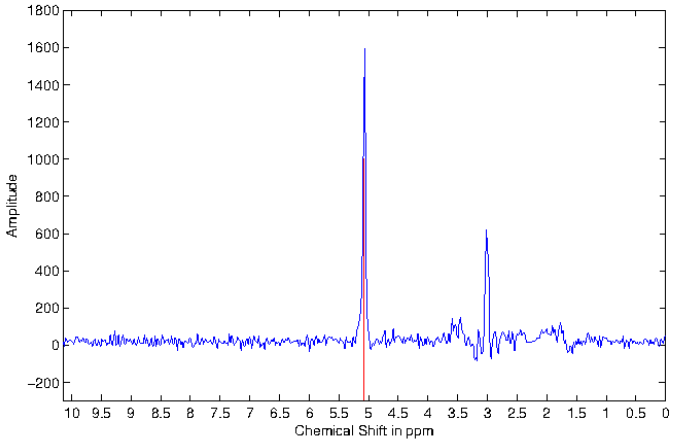

Figure 3.7: Illustration of frequency misalignment in an MRSI spectra acquired with a 3.0 Tesla MRSI scanner. The water peak is known to be aligned at 4.65 ppm. However, it can be seen that the peak on this spectra is aligned at around 5.1 ppm.

minimizing the frequency error between the experimental and theoretical values of each of these peaks.

– ***Normalization:*** Due to variations of the experimental conditions, the MRSI signal may also vary between patients. Parfait *et al.* (133) as in (177) compared two methods to normalize MRSI signal. In each method, the original MRSI spectra is divided by a normalization factor, similar to the intensity normalization described earlier. The first approach to obtain the normalization factor is based on an estimation of the water concentration. It is required to have an additional MRSI sequence where the water metabolites are unsuppressed. Using this sequence, an estimation of the water concentration can be performed using the previously reported HSVD algorithm. The second approach to normalization is based on using the L_2 norm of the MRSI spectra $\|s(\xi)\|_2$. It should be noted that both (133) and (177) concluded that the L_2 normalization was more efficient in their framework.

3.1.1.2 Segmentation

The segmentation task consists of delineating the prostate boundaries in the MRI and is of particular importance for focusing the posterior processing on the organ of interest (178). In this section, only the segmentation methods used in CAD for CaP are presented and summarized in Table. 3.3. These methods are mostly intensity based. An exhaustive review of prostate segmentation methods in MRI can be found in (178).

– ***Manual segmentation:*** To highlight the importance of prostate segmentation task in CAD systems, it is interesting to note the large number of studies which manually

Table 3.2: Overview of the pre-processing methods used in CAD systems.

Pre-processing operations	**References**
MRI pre-processing:	
Noise filtering:	
Median filtering	[20-21]
Wavelet-based filtering	[1-2,14]
Bias correction:	
Parametric methods	[15-35]
Non-parametric methods	[36]
Standardization:	
Statistical-based normalization:	[3-4,15,20-21,35,37]
Organ SI-based normalization	[18-19]
MRSI pre-processing:	
Phase correction	[22]
Water and lipid residuals filtering	[8]
Baseline correction	[22,31]
Frequency alignment	[31]
Normalization	[22]

Table 3.3: Overview of the segmentation methods used in CAD systems.

Segmentation methods	**References**
MRI-based segmentation:	
Manual segmentation	[4-5,16,18-21,24,38-40]
Region-based segmentation	[11]
Hybrid segmentation	[10,34-36,41]
MRSI-based segmentation:	
Clustering	[28]

segment the prostate organs (2, 3, 117, 118, 129, 131, 132, 134, 148, 149). In all the cases, the boundaries of the prostate gland are manually defined in order to limit further processing to only this area. This approach ensures the right delineation of the organ nevertheless this procedure is highly time consuming and should be performed by a radiologist.

- ***Region-based segmentation:*** Litjens *et al.* in (124) used a multi-atlas-based segmentation using multi-modal images (e.g., T_2-W-MRI and ADC map) to segment the prostate with an additional pattern recognition method to differentiate CG and PZ as proposed in (179). This method consists in three different steps: (i) the registration between each atlas and the multi-modal images, (ii) the atlas selection and finally (iii) the classification of the prostate segmented voxels in either CG or PZ. The registration between each atlas and the MRI images is performed using two successive registrations; the first registration is a rigid registration to roughly aligned the atlases and the MRI images and the second is an elastic registration using B-spline transformation. The objective function to perform the registration is defined as the weighted sum of the metric of both T_2-W-MRI and ADC map. The metric is based on mutual information (MI) (please refer to the next section for more details in regard to registration). Two strategies of atlas selection were performed by using either a majority voting approach or the simultaneous truth and performance level estimation (STAPLE) approach (180). After segmentation of the prostate, the differentiation of both CG and PZ has to be carried out. This problem was carried out by classifying each voxel using linear discriminant analysis (LDA). Three types of features were considered: (i) anatomy, (ii) intensity and (iii) texture. Regarding the anatomy, relative position and relative distance from the pixel to the border of the prostate were used. The intensity features consist in the intensity of the voxel in the ADC coefficient and the T_2 map. The texture features were composed of five different features: homogeneity, correlation (181), entropy, texture strength (182) and local binary pattern (LBP) (183). Finally, some morphological operations were applied to remove artefact and the contour between the zones were smooth using the thin plate spline (TPS) (184).

  Litjens *et al.* in (185) used an almost identical algorithm proposed by PROMISE12 challange (186). Their segmentation method is also based on multi-atlas multi-modal images, but the SIMPLE method (187) is used instead to combine labels after the registration of the different atlas to obtain the final segmentation.

- ***Hybrid-based segmentation:*** Viswanath *et al.* in (144, 145) used a multi-attribute non-initializing texture reconstruction based active shape model (MANTRA) method as proposed in (188). MANTRA is closely related to the active shape model (ASM) from (189). This algorithm consists of two stages: (i) a training stage where a shape and appearance model is generated and (ii) the actual segmentation performed based on the learned model. For the training stage, a set of landmarks is defined and the shape model is generated as in the original ASM method (189). **Check what is commented in the segmentation.tex here, it was not explained well so I**

didnt included them.

Litjens *et al.* (123) and Vos *et al.* (151) used an approach proposed in (190) in which the bladder, prostate and rectum are segmented.

The segmentation task is performed as an optimization problem taking three parameters into account linked to organs such as: (i) the shape (an ellipse), (ii) the location and (iii) the respective angles between them. Furthermore, Litjens *et al.* (123) used only ADC map to encode the appearance whereas Vos *et al.* (151) used both ADC and T_2 maps.

Only the work of Tiwari *et al.* in (138) propose a segmentation based on MRSI. Authors localized the voxels corresponding to the prostate organ using a hierarchical spectral clustering. First, each MRSI spectrum is projected into a lower dimension space using graph embedding (191). To proceed, a similarity matrix W is computed using a Gaussian similarity measure from Euclidean distance (192)) such that:

$$W(\mathbf{x},\mathbf{y}) = \begin{cases} \exp\left(\frac{\|s(\mathbf{x})-s(\mathbf{y})\|_2^2}{\sigma^2}\right) , & \text{if } \|\mathbf{x}-\mathbf{y}\|_2 < \epsilon , \\ 0 , & \text{if } \|\mathbf{x}-\mathbf{y}\|_2 > \epsilon . \end{cases} \tag{3.17}$$

where $s(\mathbf{x})$ and $s(\mathbf{y})$ are the MRSI spectra for the voxels $\mathbf{x}$ and $\mathbf{y}$ respectively, σ is the standard deviation of the Gaussian similarity measure and ϵ is the parameter to defined an ϵ-neighbourhood. The projection can be performed as a generalized eigenvector problem such that:

$$\begin{aligned} Lu &= \lambda D u , \\ D(\mathbf{x},\mathbf{x}) &= \sum_{\mathbf{y}} W(\mathbf{x},\mathbf{y}) , \\ L &= D - W . \end{aligned} \tag{3.18}$$

where D is the diagonal weight matrix, L is the Laplacian matrix, λ and u represent the eigenvalues and eigenvectors. Once that the MRSI spectra are projected into the lower dimension space, a replicate k-means clustering method is used to define two clusters where the larger cluster is assimilated to be the cluster corresponding to non-prostate voxels and will be eliminated. The full procedure is repeated until the total number of voxels left is inferior to a given number.

References

[1] L. G. Nyul, J. K. Udupa, and X. Zhang. **New variants of a method of MRI scale standardization**. *IEEE Trans Med Imaging*, **19**(2):143–150, Feb 2000. ix, 30, 31

[2] E. Niaf, O. Rouvire, and C. Lartizien. **Computer-aided diagnosis for prostate cancer detection in the peripheral zone via multisequence MRI**. In *Proc. SPIE 7963, Medical Imaging 2011: Computer-Aided Diagnosis*, 2011. ix, 24, 31, 32, 37

[3] E. Niaf, O. Rouviere, F. Mege-Lechevallier, F. Bratan, and C. Lartizien. **Computer-aided diagnosis of prostate cancer in the peripheral zone using multiparametric MRI**. *Phys Med Biol*, **57**(12):3833–3851, Jun 2012. ix, 24, 31, 32, 37

[4] Y. J. Choi, J. K. Kim, N. Kim, K. W. Kim, E. K. Choi, and K. S. Cho. **Functional MR imaging of prostate cancer**. *Radiographics*, **27**:63–75, 2007. 2, 11, 12, 14, 15, 16, 18, 19

[5] K. H. Leissner and L. E. Tisell. **The weight of the human prostate**. *Scand. J. Urol. Nephrol.*, **13**(2):137–142, 1979. 1

[6] S. Parfait. *Classification de spectres et recherche de biomarqueurs en spectroscopie par résonqnce magnétique nulcléaire du proton dans les tumeurs prostatiques.* PhD thesis, Université de Bourgogne, 2010. 1, 3, 4, 18

[7] J. E. McNeal. **The zonal anatomy of the prostate**. *Prostate*, **2**:35–49, 1981. 1

[8] H. Hricak, G. C. Dooms, J. E. McNeal, A. S. Mark, M. Marotti, A. Avallone, M. Pelzer, E. C. Proctor, and E. A. Tanagho. **MR imaging of the prostate gland: normal anatomy**. *AJR Am J Roentgenol*, **148**:51–58, Jan 1987. 2, 10, 11

[9] A. Villers, A. Steg, and L. Boccon-Gibod. **Anatomy of the prostate: review of the different models**. *Eur. Urol.*, **20**:261–268, 1991. 2

[10] F. V. Coakley and H. Hricak. **Radiologic anatomy of the prostate gland: a clinical approach**. *Radiol. Clin. North Am.*, **38**:15–30, Jan 2000. 2

[11] J. Ferlay, H. R. Shin, F. Bray, D. Forman, C. Mathers, and D. M. Parkin. **Estimates of worldwide burden of cancer in 2008: GLOBOCAN 2008**. *Int. J. Cancer*, **127**(12):2893–2917, Dec 2010. 2

[12] R. Siegel, D. Naishadham, and A. Jemal. **Cancer statistics, 2013**. *CA Cancer J Clin*, **63**(1):11–30, Jan 2013. 3

[13] A. C. American Cancer Society. **Cancer Facts and Figures 2013**. http://www.cancer.org/research/cancerfactsfigures, 2013. Accessed: 2013-08-01. 3

[14] A. C. American Cancer Society. **Cancer Facts and Figures 2010**. http://www.cancer.org/research/cancerfactsfigures, 2010. Accessed: 2013-08-01. 3

[15] E. Giovannucci, Y. Liu, E. A. Platz, M. J. Stampfer, and W. C. Willett. **Risk factors for prostate cancer incidence and progression in the health professionals follow-up study**. *Int. J. Cancer*, **121**(7):1571–1578, Oct 2007. 3

[16] G. D. Steinberg, B. S. Carter, T. H. Beaty, B. Childs, and P. C. Walsh. **Family history and the risk of prostate cancer**. *Prostate*, **17**(4):337–347, 1990. 3

[17] M. L. Freedman, C. A. Haiman, N. Patterson, G. J. McDonald, A. Tandon, A. Waliszewska, K. Penney, R. G. Steen, K. Ardlie, E. M. John, I. Oakley-Girvan, A. S. Whittemore, K. A. Cooney, S. A. Ingles, D. Altshuler, B. E. Henderson, and D. Reich. **Admixture mapping identifies 8q24 as a prostate cancer risk locus in African-American men**. *Proc. Natl. Acad. Sci. U.S.A.*, **103**(38):14068–14073, Sep 2006. 3

[18] L. T. Amundadottir, P. Sulem, J. Gudmundsson, A. Helgason, A. Baker, B. A. Agnarsson, A. Sigurdsson, K. R. Benediktsdottir, J. B. Cazier, J. Sainz, M. Jakobsdottir, J. Kostic, D. N. Magnusdottir, S. Ghosh, K. Agnarsson, B. Birgisdottir, L. Le Roux, A. Olafsdottir, T. Blondal, M. Andresdottir, O. S. Gretarsdottir, J. T. Bergthorsson, D. Gudbjartsson, A. Gylfason, G. Thorleifsson, A. Manolescu, K. Kristjansson, G. Geirsson, H. Isaksson, J. Douglas, J. E. Johansson, K. Balter, F. Wiklund, J. E. Montie, X. Yu, B. K. Suarez, C. Ober, K. A. Cooney, H. Gronberg, W. J. Catalona, G. V. Einarsson, R. B. Barkardottir, J. R. Gulcher, A. Kong, U. Thorsteinsdottir, and K. Stefansson. **A common variant associated with prostate cancer in European and African populations**. *Nat. Genet.*, **38**(6):652–658, Jun 2006. 3

[19] I. Agalliu, R. Gern, S. Leanza, and R. D. Burk. **Associations of high-grade prostate cancer with BRCA1 and BRCA2 founder mutations**. *Clin. Cancer Res.*, **15**(3):1112–1120, Feb 2009. 3

[20] R. M. Hoffman, F. D. Gilliland, J. W. Eley, L. C. Harlan, R. A. Stephenson, J. L. Stanford, P. C. Albertson, A. S. Hamilton, W. C. Hunt, and A. L. Potosky. **Racial and ethnic differences in advanced-stage prostate cancer: the Prostate Cancer Outcomes Study**. *J. Natl. Cancer Inst.*, **93**(5):388–395, Mar 2001. 3

[21] R. W. Ma and K. Chapman. **A systematic review of the effect of diet in prostate cancer prevention and treatment**. *J Hum Nutr Diet*, **22**(3):187–199, Jun 2009. 3

[22] D. D. Alexander, P. J. Mink, C. A. Cushing, and B. Sceurman. **A review and meta-analysis of prospective studies of red and processed meat intake and prostate cancer**. *Nutr J*, **9**:50, 2010. 3

REFERENCES

[23] C. Rodriguez, S. J. Freedland, A. Deka, E. J. Jacobs, M. L. McCullough, A. V. Patel, M. J. Thun, and E. E. Calle. **Body mass index, weight change, and risk of prostate cancer in the Cancer Prevention Study II Nutrition Cohort**. *Cancer Epidemiol. Biomarkers Prev.*, **16**(1):63–69, Jan 2007. 3

[24] S.B. Strum and D. Pogliano. **What every doctor who treats male patients should know**. PCRI Insights vol. 8, no. 2, May 2005. 3

[25] G. L. Lu-Yao, P. C. Albertsen, D. F. Moore, W. Shih, Y. Lin, R. S. DiPaola, M. J. Barry, A. Zietman, M. O'Leary, E. Walker-Corkery, and S. L. Yao. **Outcomes of localized prostate cancer following conservative management**. *JAMA*, **302**(11):1202–1209, Sep 2009. 3

[26] G. Oster, L. Lamerato, A. G. Glass, K. E. Richert-Boe, A. Lopez, K. Chung, A. Richhariya, T. Dodge, G. G. Wolff, A. Balakumaran, and J. Edelsberg. **Natural history of skeletal-related events in patients with breast, lung, or prostate cancer and metastases to bone: a 15-year study in two large US health systems**. *Support Care Cancer*, **21**(12):3279–3286, Dec 2013. 3

[27] L. Ye, H. G. Kynaston, and W. G. Jiang. **Bone metastasis in prostate cancer: molecular and cellular mechanisms (Review)**. *Int. J. Mol. Med.*, **20**(1):103–111, Jul 2007. 3

[28] C. L. Carrol, F. G. Sommer, J. E. McNeal, and T. A. Stamey. **The abnormal prostate: MR imaging at 1.5 T with histopathologic correlation**. *Radiology*, **163**(2):521–525, May 1987. 3

[29] J. E. McNeal, E. A. Redwine, F. S. Freiha, and T. A. Stamey. **Zonal distribution of prostatic adenocarcinoma. Correlation with histologic pattern and direction of spread**. *Am. J. Surg. Pathol.*, **12**(12):897–906, Dec 1988. 3

[30] T. A. Stamey, A. N. Donaldson, C. E. Yemoto, J. E. McNeal, S. Sozen, and H. Gill. **Histological and clinical findings in 896 consecutive prostates treated only with radical retropubic prostatectomy: epidemiologic significance of annual changes**. *J. Urol.*, **160**(6 Pt 2):2412–2417, Dec 1998. 3

[31] R. J. Cohen, B. A. Shannon, M. Phillips, R. E. Moorin, T. M. Wheeler, and K. L. Garrett. **Central zone carcinoma of the prostate gland: a distinct tumor type with poor prognostic features**. *J. Urol.*, **179**(5):1762–1767, May 2008. 3

[32] R. Etzioni, D. F. Penson, J. M. Legler, D. di Tommaso, R. Boer, P. H. Gann, and E. J. Feuer. **Overdiagnosis due to prostate-specific antigen screening: lessons from U.S. prostate cancer incidence trends**. *J. Natl. Cancer Inst.*, **94**(13):981–990, Jul 2002. 3

[33] C. M. Hoeks, J. O. Barentsz, T. Hambrock, D. Yakar, D. M. Somford, S. W. Heijmink, T. W. Scheenen, P. C. Vos, H. Huisman, I. M. van Oort, J. A. Witjes, A. Heerschap, and J. J. Futterer. **Prostate cancer: multiparametric MR imaging for detection, localization, and staging**. *Radiology*, **261**(1):46–66, Oct 2011. 3, 4, 10, 11, 13, 14, 18

[34] J. O. Barentsz, J. Richenberg, R. Clements, P. Choyke, S. Verma, G. Villeirs, O. Rouviere, V. Logager, and J. J. Futterer. **ESUR prostate MR guidelines 2012**. *Eur Radiol*, **22**(4):746–757, Apr 2012. 4, 7, 10, 11, 15, 16, 19

[35] D. F. Gleason. *Urologic pathology: The prostate*, chapter The Veteran's Administration Cooperative Urologic Research Group: histologic grading and clinical staging of prostatic carcinoma, page 171198. Lea and Febiger., 1977. 4

[36] J. I. Epstein, W. C. Allsbrook, M. B. Amin, and L. L. Egevad. **The 2005 International Society of Urological Pathology (ISUP) Consensus Conference on Gleason Grading of Prostatic Carcinoma**. *Am. J. Surg. Pathol.*, **29**(9):1228–1242, Sep 2005. 4

[37] N. Hara, M. Okuizumi, H. Koike, M. Kawaguchi, and V. Bilim. **Dynamic contrast-enhanced magnetic resonance imaging (DCE-MRI) is a useful modality for the precise detection and staging of early prostate cancer**. *Prostate*, **62**(2):140–147, Feb 2005. 4

[38] R. Chou, J. M. Croswell, T. Dana, C. Bougatsos, I. Blazina, R. Fu, K. Gleitsmann, H. C. Koenig, C. Lam, A. Maltz, J. B. Rugge, and K. Lin. **Screening for prostate cancer: a review of the evidence for the U.S. Preventive Services Task Force**. *Ann. Intern. Med.*, **155**(11):762–771, Dec 2011. 4

[39] Gerald L. Andriole, E. David Crawford, Robert L. Grubb, Saundra S. Buys, David Chia, Timothy R. Church, Mona N. Fouad, Edward P. Gelmann, Paul A. Kvale, Douglas J. Reding, Joel L. Weissfeld, Lance A. Yokochi, Barbara O'Brien, Jonathan D. Clapp, Joshua M. Rathmell, Thomas L. Riley, Richard B. Hayes, Barnett S. Kramer, Grant Izmirlian, Anthony B. Miller, Paul F. Pinsky, Philip C. Prorok, John K. Gohagan, and Christine D. Berg. **Mortality results from a randomized Prostate-cancer screening trial**. *New England Journal of Medicine*, **360**(13):1310–1319, 2009. 4

[40] Fritz H. Schröder, Jonas Hugosson, Monique J. Roobol, Teuvo L.J. Tammela, Stefano Ciatto, Vera Nelen, Maciej Kwiatkowski, Marcos Lujan, Hans Lilja, Marco Zappa, Louis J. Denis, Franz Recker, Alvaro Pez, Liisa Määttänen, Chris H. Bangma, Gunnar Aus, Sigrid Carlsson, Arnauld Villers, Xavier Rebillard, Theodorus van der Kwast, Paula M. Kujala, Bert G. Blijenberg, Ulf-Hakan Stenman, Andreas Huber, Kimmo Taari, Matti Hakama, Sue M. Moss, Harry J. de Koning, and Anssi Auvinen. **Prostate-cancer mortality at 11 years of follow-up**. *New England Journal of Medicine*, **366**(11):981–990, 2012. 4

[41] J. Hugosson, S. Carlsson, G. Aus, S. Bergdahl, A. Khatami, P. Lodding, C. G. Pihl, J. Stranne, E. Holmberg, and H. Lilja. **Mortality results from the Göteborg randomised population-based prostate-cancer screening trial**. *Lancet Oncol.*, **11**(8):725–732, Aug 2010. 4

[42] A. Heidenreich, P. A. Abrahamsson, W. Artibani, J. Catto, F. Montorsi, H. Van Poppel, M. Wirth, and N. Mottet. **Early detection of prostate cancer: European Association of Urology recommendation**. *Eur. Urol.*, **64**(3):347–354, Sep 2013. 4

[43] F. H. Schroder, H. B. Carter, T. Wolters, R. C. van den Bergh, C. Gosselaar, C. H. Bangma, and M. J. Roobol. **Early detection of prostate cancer in 2007. Part 1: PSA and PSA kinetics**. *Eur. Urol.*, **53**(3):468–477, Mar 2008. 4

[44] C. Delpierre, S. Lamy, M. Kelly-Irving, F. Molinie, M. Velten, B. Tretarre, A. S. Woronoff, A. Buemi, B. Lapotre-Ledoux, S. Bara, A. V. Guizard, M. Colonna, and P. Grosclaude. **Life expectancy estimates as a key factor in over-treatment: the case of prostate cancer**. *Cancer Epidemiol*, **37**(4):462–468, Aug 2013. 4

[45] A. Bourdoumis, A. G. Papatsoris, M. Chrisofos, E. Efstathiou, A. Skolarikos, and C. Deliveliotis. **The novel prostate cancer antigen 3 (PCA3) biomarker**. *Int Braz J Urol*, **36**(6):665–668, 2010. 4

[46] R. Morgan, A. Boxall, A. Bhatt, M. Bailey, R. Hindley, S. Langley, H. C. Whitaker, D. E. Neal, M. Ismail, H. Whitaker, N. Annels, A. Michael, and H. Pandha. **Engrailed-2 (EN2): a tumor specific urinary biomarker for the early diagnosis of prostate cancer**. *Clin. Cancer Res.*, **17**(5):1090–1098, Mar 2011. 4

[47] J.Chad Brenner, ArulM. Chinnaiyan, and ScottA. Tomlins. **ETS fusion genes in prostate cancer**. In Donald J. Tindall, editor, *Prostate Cancer*, **16** of *Protein Reviews*, pages 139–183. Springer New York, 2013. 4

[48] C. M. Moore, A. Ridout, and M. Emberton. **The role of MRI in active surveillance of prostate cancer**. *Curr Opin Urol*, **23**(3):261–267, May 2013. 4

[49] M. Noguchi, T. A. Stamey, J. E. McNeal, and C. M. Yemoto. **Relationship between systematic biopsies and histological features of 222 radical prostatectomy specimens: lack of prediction of tumor significance for men with nonpalpable prostate cancer**. *J. Urol.*, **166**(1):104–109, Jul 2001. 5

[50] G. P. Haas, N. B. Delongchamps, R. F. Jones, V. Chandan, A. M. Serio, A. J. Vickers, M. Jumbelic, G. Threatte, R. Korets, H. Lilja, and G. de la Roza. **Needle biopsies on autopsy prostates: sensitivity of cancer detection based on true prevalence**. *J. Natl. Cancer Inst.*, **99**(19):1484–1489, Oct 2007. 5

[51] A. V. Taira, G. S. Merrick, R. W. Galbreath, H. Andreini, W. Taubenslag, R. Curtis, W. M. Butler, E. Adamovich, and K. E. Wallner. **Performance of transperineal template-guided mapping biopsy in detecting prostate cancer in the initial and repeat biopsy setting**. *Prostate Cancer Prostatic Dis.*, **13**(1):71–77, Mar 2010. 5

[52] N. B. Delongchamps, M. Peyromaure, A. Schull, F. Beuvon, N. Bouazza, T. Flam, M. Zerbib, N. Muradyan, P. Legman, and F. Cornud. **Prebiopsy magnetic resonance imaging and prostate cancer detection: comparison of random and targeted biopsies**. *J. Urol.*, **189**(2):493–499, Feb 2013. 5

[53] M. L. Giger, H. P. Chan, and J. Boone. **Anniversary paper: History and status of CAD and quantitative image analysis: the role of Medical Physics and AAPM**. *Med Phys*, **35**(12):5799–5820, Dec 2008. 5, 21

[54] T. Hambrock, P. C. Vos, C. A. Hulsbergen-van de Kaa, J. O. Barentsz, and H. J. Huisman. **Prostate cancer: computer-aided diagnosis with multiparametric 3-T MR imaging–effect on observer performance**. *Radiology*, **266**(2):521–530, Feb 2013. 5, 6

[55] H. P. Chan, B. Sahiner, M. A. Helvie, N. Petrick, M. A. Roubidoux, T. E. Wilson, D. D. Adler, C. Paramagul, J. S. Newman, and S. Sanjay-Gopal. **Improvement of radiologists' characterization of mammographic masses by using computer-aided diagnosis: an ROC study**. *Radiology*, **212**(3):817–827, Sep 1999. 6

[56] J. C. Dean and C. C. Ilvento. **Improved cancer detection using computer-aided detection with diagnostic and screening mammography: prospective study of 104 cancers**. *AJR Am J Roentgenol*, **187**(1):20–28, Jul 2006. 6

[57] F. Li, M. Aoyama, J. Shiraishi, H. Abe, Q. Li, K. Suzuki, R. Engelmann, S. Sone, H. Macmahon, and K. Doi. **Radiologists' performance for differentiating benign from malignant lung nodules on high-resolution CT using computer-estimated likelihood of malignancy**. *AJR Am J Roentgenol*, **183**(5):1209–1215, Nov 2004. 6

[58] N. Petrick, M. Haider, R. M. Summers, S. C. Yeshwant, L. Brown, E. M. Iuliano, A. Louie, J. R. Choi, and P. J. Pickhardt. **CT colonography with computer-aided detection as a second reader: observer performance study**. *Radiology*, **246**(1):148–156, Jan 2008. 6

[59] J. V. Hegde, R. V. Mulkern, L. P. Panych, F. M. Fennessy, A. Fedorov, S. E. Maier, and C. M. Tempany. **Multiparametric MRI of prostate cancer: an update on state-of-the-art techniques and their performance in detecting and localizing prostate cancer**. *J Magn Reson Imaging*, **37**(5):1035–1054, May 2013. 6, 11

[60] H. Hricak, R. D. Williams, D. B. Spring, K. L. Moon, M. W. Hedgcock, R. A. Watson, and L. E. Crooks. **Anatomy and pathology of the male pelvis by magnetic resonance imaging**. *AJR Am J Roentgenol*, **141**(6):1101–1110, Dec 1983. 6, 7, 10

[61] R. A. Huch Boni, J. A. Boner, U. M. Lutolf, F. Trinkler, D. M. Pestalozzi, and G. P. Krestin. **Contrast-enhanced endorectal coil MRI in local staging of prostate carcinoma**. *J Comput Assist Tomogr*, **19**(2):232–237, 1995. 6

[62] J. Kurhanewicz, D. B. Vigneron, H. Hricak, P. Narayan, P. Carroll, and S. J. Nelson. **Three-dimensional H-1 MR spectroscopic imaging of the in situ human prostate with high (0.24-0.7-cm3) spatial resolution**. *Radiology*, **198**(3):795–805, Mar 1996. 6

[63] J. Scheidler, R. Petsch, U. Muller-Lisse, A.F. Heuck, and M. Reiser. **Echo-planar diffusion-weighted MR imaging of the prostate**. In *Proceedings of the 7th Annual Meeting of ISMRM Philadelphia*, page 1103, 1999. 6, 11, 13

[64] M. G. Swanson, D. B. Vigneron, T. K. Tran, N. Sailasuta, R. E. Hurd, and J. Kurhanewicz. **Single-voxel oversampled J-resolved spectroscopy of in vivo human prostate tissue**. *Magn Reson Med*, **45**(6):973–980, Jun 2001. 6

[65] B. Turkbey and P. L. Choyke. **Multiparametric MRI and prostate cancer diagnosis and risk stratification**. *Curr Opin Urol*, **22**(4):310–315, Jul 2012. 7

[66] O. Akin, E. Sala, C. S. Moskowitz, K. Kuroiwa, N. M. Ishill, D. Pucar, P. T. Scardino, and H. Hricak. **Transition zone prostate cancers: features, detection, localization, and staging at endorectal MR imaging**. *Radiology*, **239**(3):784–792, Jun 2006. 10

[67] L. Wang, Y. Mazaheri, J. Zhang, N. M. Ishill, K. Kuroiwa, and H. Hricak. **Assessment of biologic aggressiveness of prostate cancer: correlation of MR signal intensity with Gleason grade after radical prostatectomy**. *Radiology*, **246**(1):168–176, Jan 2008. 10

[68] A. P. Kirkham, M. Emberton, and C. Allen. **How good is MRI at detecting and characterising cancer within the prostate?** *Eur. Urol.*, **50**(6):1163–1174, Dec 2006. 10, 16

[69] L. E. Quint, J. S. Van Erp, P. H. Bland, S. H. Mandell, E. A. Del Buono, H. B. Grossman, G. M. Glazer, and P. W. Gikas. **Carcinoma of the prostate: MR images obtained with body coils do not accurately reflect tumor volume**. *AJR Am J Roentgenol*, **156**(3):511–516, Mar 1991. 11

[70] M. Cruz, K. Tsuda, Y. Narumi, Y. Kuroiwa, T. Nose, Y. Kojima, A. Okuyama, S. Takahashi, K. Aozasa, J. O. Barentsz, and H. Nakamura. **Characterization of low-intensity lesions in the peripheral zone of prostate on prebiopsy endorectal coil MR imaging**. *Eur Radiol*, **12**(2):357–365, Feb 2002. 11

[71] W. Liu, B. Turkbey, J. Senegas, S. Remmele, S. Xu, J. Kruecker, M. Bernardo, B. J. Wood, P. A. Pinto, and P. L. Choyke. **Accelerated T2 mapping for characterization of prostate cancer**. *Magn Reson Med*, **65**(5):1400–1406, May 2011. 11

[72] G. P. Liney, M. Lowry, L. W. Turnbull, D. J. Manton, A. J. Knowles, S. J. Blackband, and A. Horsman. **Proton MR T2 maps correlate with the citrate concentration in the prostate**. *NMR Biomed*, **9**(2):59–64, Apr 1996. 11

[73] G. P. Liney, L. W. Turnbull, M. Lowry, L. S. Turnbull, A. J. Knowles, and A. Horsman. **In vivo quantification of citrate concentration and water T2 relaxation time of the pathologic prostate gland using 1H MRS and MRI**. *Magn Reson Imaging*, **15**(10):1177–1186, 1997. 11

[74] G. P. Liney, A. J. Knowles, D. J. Manton, L. W. Turnbull, S. J. Blackband, and A. Horsman. **Comparison of conventional single echo and multi-echo sequences with a fast spin-echo sequence for quantitative T2 mapping: application to the prostate**. *J Magn Reson Imaging*, **6**(4):603–607, 1996. 11

[75] P. Gibbs, D. J. Tozer, G. P. Liney, and L. W. Turnbull. **Comparison of quantitative T2 mapping and diffusion-weighted imaging in the normal and pathologic prostate**. *Magn Reson Med*, **46**(6):1054–1058, Dec 2001. 11

[76] IngridS. Gribbestad, KjellI. Gjesdal, Gunnar Nilsen, Steinar Lundgren, MariH.B. Hjelstuen, and Alan Jackson. **An introduction to dynamic contrast-enhanced MRI in oncology**. In Alan Jackson, DavidL. Buckley, and GeoffreyJ.M. Parker, editors, *Dynamic Contrast-Enhanced Magnetic Resonance Imaging in Oncology*, Medical Radiology, pages 1–22. Springer Berlin Heidelberg, 2005. 11, 12

[77] A. R. Padhani. **Dynamic contrast-enhanced MRI in clinical oncology: current status and future directions**. *J Magn Reson Imaging*, **16**(4):407–422, Oct 2002. 11

[78] D. L. Buckley, C. Roberts, G. J. Parker, J. P. Logue, and C. E. Hutchinson. **Prostate cancer: evaluation of vascular characteristics with dynamic contrast-enhanced T1-weighted MR imaging–initial experience**. *Radiology*, **233**(3):709–715, Dec 2004. 11

[79] C. G. van Niekerk, J. A. van der Laak, M. E. Borger, H. J. Huisman, J. A. Witjes, J. O. Barentsz, and C. A. Hulsbergen-van de Kaa. **Computerized whole slide quantification shows increased microvascular density in pT2 prostate cancer as compared to normal prostate tissue**. *Prostate*, **69**(1):62–69, Jan 2009. 11

[80] C. G. van Niekerk, J. A. Witjes, J. O. Barentsz, J. A. van der Laak, and C. A. Hulsbergen-van de Kaa. **Microvascularity in transition zone prostate tumors resembles normal prostatic tissue**. *Prostate*, **73**(5):467–475, Apr 2013. 12, 13

[81] P. Carmeliet and R. K. Jain. **Angiogenesis in cancer and other diseases**. *Nature*, **407**(6801):249–257, Sep 2000. 12

[82] S. Verma, B. Turkbey, N. Muradyan, A. Rajesh, F. Cornud, M. A. Haider, P. L. Choyke, and M. Harisinghani. **Overview of dynamic contrast-enhanced MRI in prostate cancer diagnosis and management**. *AJR Am J Roentgenol*, **198**(6):1277–1288, Jun 2012. 12, 13

[83] P.S. Tofts. **T1-weighted DCE imaging concepts: modelling, acquisition and analysis**. In *Magneton Flash*. Siemens, 2010. 12, 13

[84] S.S. Kety. **The theory and applications of the exchange of inert gas at the lungs and tissues**. *Pharmacol. Rev.*, **3**(1):1–41, Mar 1951. 13

[85] P. S. Tofts. **Modeling tracer kinetics in dynamic Gd-DTPA MR imaging**. *J Magn Reson Imaging*, **7**(1):91–101, 1997. 13

[86] H. B. Larsson, T. Fritz-Hansen, E. Rostrup, L. Sondergaard, P. Ring, and O. Henriksen. **Myocardial perfusion modeling using MRI**. *Magn Reson Med*, **35**(5):716–726, May 1996. 13

[87] K. S. St Lawrence and T. Y. Lee. **An adiabatic approximation to the tissue homogeneity model for water exchange in the brain: I. Theoretical derivation**. *J. Cereb. Blood Flow Metab.*, **18**(12):1365–1377, Dec 1998. 13

[88] A. B. Rosenkrantz, A. Sabach, J. S. Babb, B. W. Matza, S. S. Taneja, and F. M. Deng. **Prostate cancer: comparison of dynamic contrast-enhanced MRI techniques for localization of peripheral zone tumor**. *AJR Am J Roentgenol*, **201**(3):W471–478, Sep 2013. 13

[89] G. J. Jager, E. T. Ruijter, C. A. van de Kaa, J. J. de la Rosette, G. O. Oosterhof, J. R. Thornbury, S. H. Ruijs, and J. O. Barentsz. **Dynamic TurboFLASH subtraction technique for contrast-enhanced MR imaging of the prostate: correlation with histopathologic results**. *Radiology*, **203**(3):645–652, Jun 1997. 13

[90] J. K. Kim, S. S. Hong, Y. J. Choi, S. H. Park, H. Ahn, C. S. Kim, and K. S. Cho. **Wash-in rate on the basis of dynamic contrast-enhanced MRI: usefulness for prostate cancer detection and localization**. *J Magn Reson Imaging*, **22**(5):639–646, Nov 2005. 13

[91] H. P. Schlemmer, J. Merkle, R. Grobholz, T. Jaeger, M. S. Michel, A. Werner, J. Rabe, and G. van Kaick. **Can preoperative contrast-enhanced dynamic MR imaging for prostate cancer predict microvessel density in prostatectomy specimens?** *Eur Radiol*, **14**(2):309–317, Feb 2004. 13

[92] B. Zelhof, M. Lowry, G. Rodrigues, S. Kraus, and L. Turnbull. **Description of magnetic resonance imaging-derived enhancement variables in pathologically confirmed prostate cancer and normal peripheral zone regions**. *BJU Int.*, **104**(5):621–627, Sep 2009. 13

[93] D. Le Bihan, E. Breton, D. Lallemand, M. L. Aubin, J. Vignaud, and M. Laval-Jeantet. **Separation of diffusion and perfusion in intravoxel incoherent motion MR imaging**. *Radiology*, **168**(2):497–505, Aug 1988. 13

[94] D. M. Koh and D. J. Collins. **Diffusion-weighted MRI in the body: applications and challenges in oncology**. *AJR Am J Roentgenol*, **188**(6):1622–1635, Jun 2007. 13, 14

[95] D. M. Somford, J. J. Futterer, T. Hambrock, and J. O. Barentsz. **Diffusion and perfusion MR imaging of the prostate**. *Magn Reson Imaging Clin N Am*, **16**(4):685–695, Nov 2008. 14

[96] T. A. Huisman. **Diffusion-weighted imaging: basic concepts and application in cerebral stroke and head trauma**. *Eur Radiol*, **13**(10):2283–2297, Oct 2003. 14, 15

[97] D. Le Bihan, E. Breton, D. Lallemand, P. Grenier, E. Cabanis, and M. Laval-Jeantet. **MR imaging of intravoxel incoherent motions: application to diffusion and perfusion in neurologic disorders**. *Radiology*, **161**(2):401–407, Nov 1986. 15

[98] R. Shimofusa, H. Fujimoto, H. Akamata, K. Motoori, S. Yamamoto, T. Ueda, and H. Ito. **Diffusion-weighted imaging of prostate cancer**. *J Comput Assist Tomogr*, **29**(2):149–153, 2005. 15

[99] A. R. Padhani. **Integrating multiparametric prostate MRI into clinical practice**. *Cancer Imaging*, **11 Spec No A**:27–37, 2011. 15

[100] K. W. Doo, D. J. Sung, B. J. Park, M. J. Kim, S. B. Cho, Y. W. Oh, Y. H. Ko, and K. S. Yang. **Detectability of low and intermediate or high risk prostate cancer with combined T2-weighted and diffusion-weighted MRI**. *Eur Radiol*, **22**(8):1812–1819, Aug 2012. 16

[101] T. Hambrock, D. M. Somford, H. J. Huisman, I. M. van Oort, J. A. Witjes, C. A. Hulsbergen-van de Kaa, T. Scheenen, and J. O. Barentsz. **Relationship between apparent diffusion coefficients at 3.0-T MR imaging and Gleason grade in peripheral zone prostate cancer**. *Radiology*, **259**(2):453–461, May 2011. 16

[102] Y. Itou, K. Nakanishi, Y. Narumi, Y. Nishizawa, and H. Tsukuma. **Clinical utility of apparent diffusion coefficient (ADC) values in patients with prostate cancer: can ADC values contribute to assess the aggressiveness of prostate cancer?** *J Magn Reson Imaging*, **33**(1):167–172, Jan 2011. 16

[103] Y. Peng, Y. Jiang, C. Yang, J.B. Brown, T. Antic, I. Sethi, C. Schmid-Tannwald, M.L. Giger, S.E. Eggener, and A. Oto. **Quantitative analysis of multiparametric prostate MR images: differentiation between prostate cancer and normal tissue and correlation with Gleason score–a computer-aided diagnosis development study**. *Radiology*, **267**(1):787–796, June 2013. 16, 24

[104] H. M. Awwad, J. Geisel, and R. Obeid. **The role of choline in prostate cancer**. *Clin. Biochem.*, **45**(18):1548–1553, Dec 2012. 17

[105] L. C. Costello and R. B. Franklin. **The clinical relevance of the metabolism of prostate cancer; zinc and tumor suppression: connecting the dots**. *Mol. Cancer*, **5**:17, 2006. 17

[106] G. F. Giskeodegard, H. Bertilsson, K. M. Selnaes, A. J. Wright, T. F. Bathen, T. Viset, J. Halgunset, A. Angelsen, I. S. Gribbestad, and M. B. Tessem. **Spermine and citrate as metabolic biomarkers for assessing prostate cancer aggressiveness**. *PLoS ONE*, **8**(4):e62375, 2013. 17, 18, 19

[107] M. van der Graaf, R. G. Schipper, G. O. Oosterhof, J. A. Schalken, A. A. Verhofstad, and A. Heerschap. **Proton MR spectroscopy of prostatic tissue focused on the detection of spermine, a possible biomarker of malignant behavior in prostate cancer**. *MAGMA*, **10**(3):153–159, Jul 2000. 17, 18

[108] E.M. Haacke, R.W. Brown, M.R. Thompson, and R. Venkatesan. *Magnetic resonance imaging: Physical principles and sequence design*. Wiley, 1999. 17, 18

[109] G. Lemaître. *Absolute quantification at 3 T*. Master's thesis, Université de Bourgogne, Heriot-Watt University, Universitat de Girona, 2011. 18, 19

[110] J. Scheidler, H. Hricak, D. B. Vigneron, K. K. Yu, D. L. Sokolov, L. R. Huang, C. J. Zaloudek, S. J. Nelson, P. R. Carroll, and J. Kurhanewicz. **Prostate cancer: localization with three-dimensional proton MR spectroscopic imaging–clinicopathologic study**. *Radiology*, **213**(2):473–480, Nov 1999. 18

[111] Y. Kaji, J. Kurhanewicz, H. Hricak, D. L. Sokolov, L. R. Huang, S. J. Nelson, and D. B. Vigneron. **Localizing prostate cancer in the presence of postbiopsy changes on MR images: role of proton MR spectroscopic imaging**. *Radiology*, **206**(3):785–790, Mar 1998. 18

[112] Joan C Vilanova, Josep Comet, Carles Barceló-Vidal, Joaquim Barceló, Eugeni López-Bonet, Albert Maroto, Montse Arzoz, Àngel Moreno, and Joan Areal. **Peripheral zone prostate cancer in patients with elevated PSA levels and low free-to-total PSA ratio: detection with MR imaging and MR spectroscopy**. *Radiology*, **253**(1):135–143, 2009. 18

[113] P.M. Walker, G. Crehange, S. Parfait, A. Cochet, P. Maignon, L. Cormier, and F. Brunotte. **Absolute quantification in 1H MRSI of the prostate at 3T**. In *ISMRM Annual Meeting 2010*, 2010. 19

[114] D. Ampeliotis, A. Anonakoudi, K. Berberidis, and E. Z. Psarakis. **Computer aided detection of prostate cancer using fused information from dynamic contrast enhanced and morphological magnetic resonance images**. In *IEEE International Conference on Signal Processing and Communications*, pages 888–891, 2007. 24, 26

[115] D. Ampeliotis, A. Anonakoudi, K. Berberidis, E. Z. Psarakis, and A. Kounoudes. **A computer-aided system for the detection of prostate cancer based on magnetic resonance image analysis**. In *International Symposium on Communications, Control and Signal Processing*, 2008. 24, 26

[116] Tatjana Antic, Yahui Peng, Yulei Jiang, Maryellen L. Giger, Scott Eggener, and Aytekin Oto. **A study of T2-weighted MR image texture features and diffusion-weighted MR image features for computer-aided diagnosis of prostate cancer**. In *Proc. SPIE 8670, Medical Imaging 2013: Computer-Aided Diagnosis*, pages 86701H–86701H–6, 2013. 24

[117] Y. Artan, D.L. Langer, M.A. Haider, T. H. Van der Kwast, A.J. Evans, M.N. Wernick, and I.S. Yetik. **Prostate cancer segmentation with multispectral MRI using cost-sensitive Conditional Random Fields**. In *Biomedical Imaging: From Nano to Macro, 2009. ISBI '09. IEEE International Symposium on*, pages 278–281, 2009. 24, 29, 37

[118] Y. Artan, M. A. Haider, D. L. Langer, T. H. van der Kwast, A. J. Evans, Y. Yang, M. N. Wernick, J. Trachtenberg, and I. S. Yetik. **Prostate cancer localization with multispectral MRI using cost-sensitive support vector machines and conditional random fields**. *IEEE Trans Image Process*, **19**(9):2444–2455, Sep 2010. 24, 29, 37

[119] I. Chan, W. Wells, R. V. Mulkern, S. Haker, J. Zhang, K. H. Zou, S. E. Maier, and C. M. Tempany. **Detection of prostate cancer by integration of line-scan diffusion, T2-mapping and T2-weighted magnetic resonance imaging; a multichannel statistical classifier**. *Med Phys*, **30**(9):2390–2398, Sep 2003. 24

[120] V. Giannini, A. Vignati, S. Mazzetti, M. De Luca, C. Bracco, M. Stasi, F. Russo, E. Armando, and D. Regge. **A prostate CAD system based on multiparametric analysis of DCE T1-w, and DW automatically registered images**. In *Proc. SPIE 8670, Medical Imaging 2013: Computer-Aided Diagnosis*, pages 86703E–86703E–6, 2013. 24

[121] B. M. Kelm, B. H. Menze, C. M. Zechmann, K. T. Baudendistel, and F. A. Hamprecht. **Automated estimation of tumor probability in prostate magnetic resonance spectroscopic imaging: pattern recognition vs quantification**. *Magn Reson Med*, **57**(1):150–159, Jan 2007. 24, 33

[122] D. L. Langer, T. H. van der Kwast, A. J. Evans, J. Trachtenberg, B. C. Wilson, and M. A. Haider. **Prostate cancer detection with multi-parametric MRI: logistic regression analysis of quantitative T2, diffusion-weighted imaging, and dynamic contrast-enhanced MRI**. *J Magn Reson Imaging*, **30**(2):327–334, Aug 2009. 24

[123] G. J. S. Litjens, P. C. Vos, J. O. Barentsz, N. Karssemeijer, and H. J. Huisman. **Automatic computer aided detection of abnormalities in multi-parametric prostate MRI**. In *Proc. SPIE 7963, Medical Imaging 2011: Computer-Aided Diagnosis*, pages 79630T–79630T–7, 2011. 24, 38

[124] G. J. S. Litjens, J. O. Barentsz, N. Karssemeijer, and H. J. Huisman. **Automated computer-aided detection of prostate cancer in MR images: from a whole-organ to a zone-based approach**. In *Proc. SPIE 8315, Medical Imaging 2012: Computer-Aided Diagnosis*, pages 83150G–83150G–6, 2012. 24, 37

[125] X. Liu, D. L. Langer, M. A. Haider, Y. Yang, M. N. Wernick, and I. S. Yetik. **Prostate cancer segmentation with simultaneous estimation of Markov random field parameters and class**. *IEEE Trans Med Imaging*, **28**(6):906–915, Jun 2009. 24

[126] P. Liu, S. Wang, B. Turkbey, P.and Choyke P. Grant, K.and Pinto, B. J. Wood, and R. M. Summers. **A prostate cancer computer-aided diagnosis system using multimodal magnetic resonance imaging and targeted biopsy labels**. In *Proc. SPIE 8670, Medical Imaging 2013: Computer-Aided Diagnosis*, pages 86701G–86701G–6, 2013. 24, 30

[127] R. Lopes, A. Ayache, N. Makni, P. Puech, A. Villers, S. Mordon, and N. Betrouni. **Prostate cancer characterization on MR images using fractal features**. *Med Phys*, **38**(1):83–95, Jan 2011. 24, 26

[128] D. Lv, X. Guo, X. Wang, J. Zhang, and J. Fang. **Computerized characterization of prostate cancer by fractal analysis in MR images**. *J Magn Reson Imaging*, **30**(1):161–168, Jul 2009. 24, 29, 30

[129] Lukasz Matulewicz, Jacobus F.A. Jansen, Louisa Bokacheva, Hebert Alberto Vargas, Oguz Akin, Samson W. Fine, Amita Shukla-Dave, James A. Eastham, Hedvig Hricak, Jason A. Koutcher, and Kristen L. Zakian. **Anatomic segmentation improves prostate cancer detection with artificial neural networks analysis of 1H magnetic resonance spectroscopic imaging**. *Journal of Magnetic Resonance Imaging*, pages n/a–n/a, 2013. 24, 37

[130] S. Mazzetti, M. De Luca, C. Bracco, A. Vignati, V. Giannini, M. Stasi, F. Russo, E. Armando, S. Agliozzo, and D. Regge. **A CAD system based on multiparametric analysis for cancer prostate detection on DCE-MRI**. In *Proc. SPIE 7963, Medical Imaging 2011: Computer-Aided Diagnosis*, pages 79633Q–79633Q–7, 2011. 24

[131] S. Ozer, M.A. Haider, D. L. Langer, T. H. Van der Kwast, A.J. Evans, M.N. Wernick, J. Trachtenberg, and I.S. Yetik. **Prostate cancer localization with multispectral MRI based on Relevance Vector Machines**. In *Biomedical Imaging: From Nano to Macro, 2009. ISBI '09. IEEE International Symposium on*, pages 73–76, 2009. 24, 26, 29, 37

[132] S. Ozer, D. L. Langer, X. Liu, M. A. Haider, T. H. van der Kwast, A. J. Evans, Y. Yang, M. N. Wernick, and I. S. Yetik. **Supervised and unsupervised methods for prostate cancer segmentation with multispectral MRI**. *Med Phys*, **37**(4):1873–1883, Apr 2010. 24, 26, 29, 37

[133] S. Parfait, P.M. Walker, G. Crhange, X. Tizon, and J. Mitran. **Classification of prostate magnetic resonance spectra using Support Vector Machine** . *Biomedical Signal Processing and Control*, **7**(5):499 – 508, 2012. 24, 32, 34, 35

[134] P. Puech, N. Betrouni, N. Makni, A. S. Dewalle, A. Villers, and L. Lemaitre. **Computer-assisted diagnosis of prostate cancer using DCE-MRI data: design, implementation and preliminary results**. *Int J Comput Assist Radiol Surg*, **4**(1):1–10, Jan 2009. 24, 37

[135] Y. S. Sung, H. J. Kwon, B. W. Park, G. Cho, C. K. Lee, K. S. Cho, and J. K. Kim. **Prostate cancer detection on dynamic contrast-enhanced MRI: computer-aided diagnosis versus single perfusion parameter maps**. *AJR Am J Roentgenol*, **197**(5):1122–1129, Nov 2011. 24

[136] P. Tiwari, A. Madabhushi, and M. Rosen. **A hierarchical unsupervised spectral clustering scheme for detection of prostate cancer from magnetic resonance spectroscopy (MRS)**. *Med Image Comput Comput Assist Interv*, **10**(Pt 2):278–286, 2007. 24

[137] P. Tiwari, M. Rosen, and A. Madabhushi. **Consensus-locally linear embedding (C-LLE): application to prostate cancer detection on magnetic resonance spectroscopy**. *Med Image Comput Comput Assist Interv*, **11**(Pt 2):330–338, 2008. 24

[138] P. Tiwari, M. Rosen, and A. Madabhushi. **A hierarchical spectral clustering and nonlinear dimensionality reduction scheme for detection of prostate cancer from magnetic resonance spectroscopy (MRS)**. *Med Phys*, **36**(9):3927–3939, Sep 2009. 24, 38

[139] P. Tiwari, M. Rosen, G. Reed, J. Kurhanewicz, and A. Madabhushi. **Spectral embedding based probabilistic boosting tree (ScEPTre): classifying high dimensional heterogeneous biomedical data**. *Med Image Comput Comput Assist Interv*, **12**(Pt 2):844–851, 2009. 24

[140] P. Tiwari, J. Kurhanewicz, M. Rosen, and A. Madabhushi. **Semi supervised multi kernel (SeSMiK) graph embedding: identifying aggressive prostate cancer via magnetic resonance imaging and spectroscopy**. *Med Image Comput Comput Assist Interv*, **13**(Pt 3):666–673, 2010. 24

[141] P. Tiwari, S. Viswanath, J. Kurhanewicz, A. Sridhar, and A. Madabhushi. **Multimodal wavelet embedding representation for data combination (MaWERiC): integrating magnetic resonance imaging and spectroscopy for prostate cancer detection**. *NMR Biomed*, **25**(4):607–619, Apr 2012. 24, 34

[142] P. Tiwari, J. Kurhanewicz, and A. Madabhushi. **Multi-kernel graph embedding for detection, Gleason grading of prostate cancer via MRI/MRS**. *Med Image Anal*, **17**(2):219–235, Feb 2013. 24

[143] S. Viswanath, P. Tiwari, M. Rosen, and A. Madabhushi. **A meta-classifier for detecting prostate cancer by quantitative integration of *In Vivo* magnetic resonance spectroscopy and magnetic resonance imaging**. In *Medical Imaging 2008: Computer-Aided Diagnosis*, **6915**. SPIE, 2008. 24

[144] S. Viswanath, B. N. Bloch, E. Genega, N. Rofsky, R. Lenkinski, J. Chappelow, R. Toth, and A. Madabhushi. **A comprehensive segmentation, registration, and cancer detection scheme on 3 Tesla in vivo prostate DCE-MRI**. *Med Image Comput Comput Assist Interv*, **11**(Pt 1):662–669, 2008. 24, 37

[145] S. Viswanath, B. N. Bloch, M. Rosen, J. Chappelow, R. Toth, N. Rofsky, R. Lenkinski, E. Genega, A. Kalyanpur, and A. Madabhushi. **Integrating structural and functional imaging for computer assisted detection of prostate cancer on multi-protocol in vivo 3 Tesla MRI**. In *Society of Photo-Optical Instrumentation Engineers (SPIE) Conference Series*, **7260** of *Society of Photo-Optical Instrumentation Engineers (SPIE) Conference Series*, February 2009. 24, 27, 30, 37

[146] S. Viswanath, B. N. Bloch, J. Chappelow, P. Patel, N. Rofsky, R. Lenkinski, E. Genega, and A. Madabhushi. **Enhanced multi-protocol analysis via intelligent supervised embedding (EMPrAvISE): detecting prostate cancer on multi-parametric MRI**. In *Proc. SPIE 7963, Medical Imaging 2011: Computer-Aided Diagnosis*, 2011. 24, 30

[147] S. E. Viswanath, N. B. Bloch, J. C. Chappelow, R. Toth, N. M. Rofsky, E. M. Genega, R. E. Lenkinski, and A. Madabhushi. **Central gland and peripheral zone prostate tumors have significantly different quantitative imaging signatures on 3 Tesla endorectal, in vivo T2-weighted MR imagery**. *J Magn Reson Imaging*, **36**(1):213–224, Jul 2012. 24, 28, 30

[148] P. C. Vos, T. Hambrock, J. O. Barenstz, and H. J. Huisman. **Combining T2-weighted with dynamic MR images for computerized classification of prostate lesions**. In *Medical Imaging 2008: Computer-Aided Diagnosis*, **6915**. SPIE, 2008. 24, 37

[149] P. C. Vos, T. Hambrock, C. A. Hulsbergen-van de Kaa, J. J. Futterer, J. O. Barentsz, and H. J. Huisman. **Computerized analysis of prostate lesions in the peripheral zone using dynamic contrast enhanced MRI**. *Med Phys*, **35**(3):888–899, Mar 2008. 24, 37

[150] P. C. Vos, T. Hambrock, J. O. Barenstz, and H. J. Huisman. **Computer-assisted analysis of peripheral zone prostate lesions using T2-weighted and dynamic contrast enhanced T1-weighted MRI**. *Phys Med Biol*, **55**(6):1719–1734, Mar 2010. 24

[151] P. C. Vos, J. O. Barentsz, N. Karssemeijer, and H. J. Huisman. **Automatic computer-aided detection of prostate cancer based on multiparametric magnetic resonance image analysis**. *Phys Med Biol*, **57**(6):1527–1542, Mar 2012. 24, 38

[152] R.D. Nowak. **Wavelet-based Rician noise removal for magnetic resonance imaging**. *Image Processing, IEEE Transactions on*, **8**(10):1408–1419, 1999. 25, 26

[153] J. V. Manjon, J. Carbonell-Caballero, J. J. Lull, G. Garcia-Marti, L. Marti-Bonmati, and M. Robles. **MRI denoising using non-local means**. *Med Image Anal*, **12**(4):514–523, Aug 2008. 26

[154] A. Buades, B. Coll, and J.M. Morel. **A review of image denoising algorithms, with a new one**. *Simul*, **4**:490–530, 2005. 26

[155] J. Mohan, V. Krishnaveni, and Y. Guo. **A survey on the magnetic resonance image denoising methods**. *Biomedical Signal Processing and Control*, **9**(0):56 – 69, 2014. 26

[156] D. L. Donoho and J. M. Johnstone. **Ideal spatial adaptation by wavelet shrinkage**. *Biometrika*, **81**(3):425–455, 1994. 26

[157] Aleksandra Pizurica. *Image denoising using wavelets and spatial context modeling*. PhD thesis, Universiteit Gent, 2002. 26

[158] S. Mallat. *A wavelet tour of signal processing, Third Edition: The sparse way*. Academic Press, 3rd edition, 2008. 26

[159] A. Pizurica, W. Philips, I. Lemahieu, and M. Acheroy. **A versatile wavelet domain noise filtration technique for medical imaging**. *IEEE Trans Med Imaging*, **22**(3):323–331, Mar 2003. 26

[160] M. Styner, C. Brechbuhler, G. Szckely, and G. Gerig. **Parametric estimate of intensity inhomogeneities applied to MRI**. *Medical Imaging, IEEE Transactions on*, **19**(3):153–165, 2000. 27

[161] M. Jungke, W. Von Seelen, G. Bielke, S. Meindl, M. Grigat, and P. Pfannenstiel. **A system for the diagnostic use of tissue characterizing parameters in NMR-tomography**. In *Proc. of Information Processing in Medical Imaging*, **87**, pages 471–481, 1987. 27

[162] U. Vovk, F. Pernus, and B. Likar. **A review of methods for correction of intensity inhomogeneity in MRI**. *Medical Imaging, IEEE Transactions on*, **26**(3):405–421, 2007. 27

[163] S. Z. Li. **Robustizing robust M-estimation using deterministic annealing**. *Pattern Recognition*, **29**:159–166, 1996. 28

[164] M. Styner and G. Gerig. **Evaluation of 2D/3D bias correction with 1+1ES-optimization**. Technical report, ETH Zürich, 1997. 28

[165] J. G. Sled, A. P. Zijdenbos, and A. C. Evans. **A nonparametric method for automatic correction of intensity nonuniformity in MRI data**. *IEEE Trans Med Imaging*, **17**(1):87–97, Feb 1998. 28

[166] A. Madabhushi, J.K. Udupa, and A. Souza. **Generalized scale: Theory, algorithms, and application to image inhomogeneity correction** . *Computer Vision and Image Understanding*, **101**(2):100 – 121, 2006. 29

[167] L. G. Shapiro and G. C. Stockman. *Computer vision*. Prentice Hall, Upper Saddle River, NJ, 2001. 29

[168] L. G. Nyul and J. K. Udupa. **On standardizing the MR image intensity scale**. *Magn Reson Med*, **42**(6):1072–1081, Dec 1999. 29

[169] A. Madabhushi and J. K. Udupa. **New methods of MR image intensity standardization via generalized scale**. *Med Phys*, **33**(9):3426–3434, Sep 2006. 30

[170] M. Wiart, L. Curiel, A. Gelet, D. Lyonnet, J. Y. Chapelon, and O. Rouviere. **Influence of perfusion on high-intensity focused ultrasound prostate ablation: a first-pass MRI study**. *Magn Reson Med*, **58**(1):119–127, Jul 2007. 32

[171] Li Chen, Zhiqiang Weng, LaiYoong Goh, and Marc Garland. **An efficient algorithm for automatic phase correction of {NMR} spectra based on entropy minimization** . *Journal of Magnetic Resonance*, **158**(12):164 – 168, 2002. 32, 33, 34

[172] M.I. Osorio-Garcia, A.R. Croitor Sava, D. M. Sima, F.U. Nielsen, U. Himmelreich, and S. Van Huffel. *Magnetic Resonance Spectroscopy*, chapter Quantification improvements of 1H MRS Signals, pages 1–27. InTech, March 2012. 32, 33, 34

[173] H. Zhu, R. Ouwerkerk, and P. B. Barker. **Dual-band water and lipid suppression for MR spectroscopic imaging at 3 Tesla**. *Magn Reson Med*, **63**(6):1486–1492, Jun 2010. 33

[174] W.W.F Pijnappel, A van den Boogaart, R de Beer, and D van Ormondt. **SVD-based quantification of magnetic resonance signals** . *Journal of Magnetic Resonance (1969)*, **97**(1):122 – 134, 1992. 33, 34

[175] T. Laudadio, N. Mastronardi, L. Vanhamme, P. Van Hecke, and S. Van Huffel. **Improved Lanczos algorithms for blackbox {MRS} data quantitation**. *Journal of Magnetic Resonance*, **157**(2):292 – 297, 2002. 34

[176] C. A. Lieber and A. Mahadevan-Jansen. **Automated method for subtraction of fluorescence from biological Raman spectra**. *Appl Spectrosc*, **57**(11):1363–1367, Nov 2003. 34

[177] A. Devos, L. Lukas, J. A. Suykens, L. Vanhamme, A. R. Tate, F. A. Howe, C. Majos, A. Moreno-Torres, M. van der Graaf, C. Arus, and S. Van Huffel. **Classification of brain tumours using short echo time 1H MR spectra**. *J. Magn. Reson.*, **170**(1):164–175, Sep 2004. 34, 35

[178] S. Ghose, A. Oliver, R. Marti, X. Llado, J. C. Vilanova, J. Freixenet, J. Mitra, D. Sidibe, and F. Meriaudeau. **A survey of prostate segmentation methodologies in ultrasound, magnetic resonance and computed tomography images**. *Comput Methods Programs Biomed*, **108**(1):262–287, Oct 2012. 35

[179] G. Litjens, O. Debats, W. van de Ven, N. Karssemeijer, and H. Huisman. **A pattern recognition approach to zonal segmentation of the prostate on MRI**. *Med Image Comput Comput Assist Interv*, **15**(Pt 2):413–420, 2012. 37

[180] S. K. Warfield, K. H. Zou, and W. M. Wells. **Simultaneous truth and performance level estimation (STAPLE): an algorithm for the validation of image segmentation**. *IEEE Trans Med Imaging*, **23**(7):903–921, Jul 2004. 37

[181] M. Amadasun and R. King. **Textural features corresponding to textural properties**. *Systems, Man and Cybernetics, IEEE Transactions on*, **19**(5):1264–1274, 1989. 37

[182] H. Li, M. L. Giger, O. I. Olopade, A. Margolis, L. Lan, and M. R. Chinander. **Computerized texture analysis of mammographic parenchymal patterns of digitized mammograms**. *Acad Radiol*, **12**(7):863–873, Jul 2005. 37

[183] T. Ojala, M. Pietikäinen, and D. Harwood. **A comparative study of texture measures with classification based on featured distributions**. *Pattern Recognition*, **29**(1):51–59, January 1996. 37

[184] F. L. Bookstein. **Principal warps: thin-plate splines and the decomposition of deformations**. *Pattern Analysis and Machine Intelligence, IEEE Transactions on*, **11**(6):567–585, 1989. 37

[185] G. Litjens, O. Debats, J. Barentsz, N. Karssemeijer, and H. Huisman. **Computer-iided detection of prostate cancer in MRI**. *Medical Imaging, IEEE Transactions on*, **33**(5):1083–1092, May 2014. 37

[186] G. Litjens, R. Toth, W. van de Ven, C. Hoeks, S. Kerkstra, B. van Ginneken, G. Vincent, G. Guillard, N. Birbeck, J. Zhang, R. Strand, F. Malmberg, Y. Ou, C. Davatzikos, M. Kirschner, F. Jung, J. Yuan, W. Qiu, Q. Gao, P. E. Edwards, B. Maan, F. van der Heijden, S. Ghose, J. Mitra, J. Dowling, D. Barratt, H. Huisman, and A. Madabhushi. **Evaluation of prostate segmentation algorithms for MRI: the PROMISE12 challenge**. *Med Image Anal*, **18**(2):359–373, Feb 2014. 37

[187] Thomas Robin Langerak, Uulke A van der Heide, Alexis NTJ Kotte, Max A Viergever, Marco van Vulpen, and Josien PW Pluim. **Label fusion in atlas-based segmentation using a selective and iterative method for performance level estimation (SIMPLE)**. *IEEE Transactions on Medical Imaging*, **29**(12):2000–2008, 2010. 37

[188] R. Toth, J. Chappelow, M. Rosen, S. Pungavkar, A. Kalyanpur, and A. Madabhushi. **Multi-attribute non-initializing texture reconstruction based active shape model (MANTRA)**. *Med Image Comput Comput Assist Interv*, **11**(Pt 1):653–661, 2008. 37

[189] T. F. Cootes, C. J. Taylor, D. H. Cooper, and J. Graham. **Active shape models&Mdash;Their training and application**. *Comput. Vis. Image Underst.*, **61**(1):38–59, January 1995. 37

[190] H. Huisman, P.C. Vos, G. Litjens, T. Hambrock, and J. Barentsz. **Computer aided detection of prostate cancer using T2, DWI and DCE MRI: methods and clinical applications**. In *Proceedings of the 2010 international conference on Prostate cancer imaging: computer-aided diagnosis, prognosis, and intervention*, MICCAI'10, pages 4–14, Berlin, Heidelberg, 2010. Springer-Verlag. 38

[191] J. Shi and J. Malik. **Normalized cuts and image segmentation**. *Pattern Analysis and Machine Intelligence, IEEE Transactions on*, **22**(8):888–905, 2000. 38

[192] M. Belkin and P. Niyogi. **Laplacian eigenmaps and spectral techniques for embedding and clustering**. In *Advances in Neural Information Processing Systems 14*, pages 585–591. MIT Press, 2001. 38

Declaration

I herewith declare that I have produced this paper without the prohibited assistance of third parties and without making use of aids other than those specified; notions taken over directly or indirectly from other sources have been identified as such. This paper has not previously been presented in identical or similar form to any other German or foreign examination board.

The thesis work was conducted from XXX to YYY under the supervision of PI at ZZZ.

CITY,